

1

Abstract

2

Measurement of total hadronic differential cross sections in the LArIAT experiment

3

4

Elena Gramellini

5

2018

6

Abstract goes here. Limit 750 words.

7 **Measurement of total hadronic differential**
8 **cross sections in the LArIAT experiment**

9 A Dissertation
10 Presented to the Faculty of the Graduate School
11 of
12 Yale University
13 in Candidacy for the Degree of
14 Doctor of Philosophy

15 by
16 Elena Gramellini

17 Dissertation Director: Bonnie T. Fleming

18 Date you'll receive your degree

21

A mia mamma e mio babbo,

22

grazie per le radici e grazie per le ali.

23

To my mom and dad,

24

thank you for the roots and thank you for the wings.

Contents

26	Acknowledgements	vi
27	0 Total Hadronic Cross Section Measurement Methodology	1
28	0.1 Event Selection	2
29	0.1.1 Selection of Beamline Events	2
30	0.1.2 Particle Identification in the Beamline	3
31	0.1.3 TPC Selection: Halo Mitigation	3
32	0.1.4 TPC Selection: Shower Removal	4
33	0.2 Beamline and TPC Handshake: the Wire Chamber to TPC Match . .	5
34	0.3 The Thin Slice Method	7
35	0.3.1 Cross Sections on Thin Target	7
36	0.3.2 Not-so-Thin Target: Slicing the Argon	8
37	0.3.3 Corrections to the Raw Cross Section	10
38	0.4 Procedure testing with truth quantities	11
39	1 Data and MC preparation for the Cross Section Measurements	14
40	1.1 Cross Section Analyses Data Sets	14
41	1.2 Construction of a Monte Carlo Simulation for LArIAT	16
42	1.2.1 G4Beamline	16
43	1.2.2 Data Driven MC	20
44	1.3 Estimate of Backgrounds in the Pion Cross Section	22

45	1.3.1	Background from Pion Capture and Decay	24
46	1.3.2	Beamline Background	27
47	1.4	Estimate of Energy Loss before the TPC	28
48	1.5	Tracking Studies	30
49	1.5.1	Study of WC to TPC Match	33
50	1.5.2	Tracking Optimization	36
51	1.5.3	Angular Resolution	36
52	1.6	Calorimetry Studies	40
53	1.6.1	Energy Calibration	40
54	1.6.2	Kinetic Energy Measurement	42
55	2	Negative Pion Cross Section Measurement	46
56	2.1	Raw Cross Section	46
57	2.1.1	Statistical Uncertainty	48
58	2.1.2	Treatment of Systematics	50
59	2.2	Corrections to the Raw Cross Section	51
60	2.2.1	Background subtraction	51
61	2.2.2	Background Contribution to the Cross Section	54
62	2.2.3	Efficiency Correction	54
63	2.3	Results	59

Acknowledgements

*“Dunque io ringrazio tutti quanti.
Specie la mia mamma che mi ha fatto così funky.”*
– Articolo 31, Tanqi Funky, 1996 –

*“At last, I thank everyone.
Especially my mom who made me so funky.”*
– Articolo 31, Tanqi Funky, 1996 –

A lot of people are awesome, especially you, since you probably agreed to read this when it was a draft.

Chapter 0

Total Hadronic Cross Section Measurement Methodology

This chapter describes the general procedure employed to measure a total hadronic differential cross section in LArIAT. Albeit with small differences, both the (π^-, Ar) and (K^+, Ar) total hadronic cross section measurements rely on the same procedure described in details in the following sections. We start by selecting the particle of interest using a combination of beamline detectors and TPC information (Section 0.1). We then perform a handshake between the beamline information and the TPC tracking to assure the selection of the right TPC track (Section 0.2). Finally, we apply the “thin slice” method and measure the “raw” hadronic cross section (Section 0.3). A series of corrections are then evaluated to obtain the “true” cross section (Section 0.3.3).

At the end of this chapter, we show a sanity check of the methodology by applying the thin slice method employing only MC truth information and retrieving the Geant4 tabulated cross section for pions and kaons (Section 0.4).

0.1 Event Selection

The measurement of the (π^- ,Ar) and (K^+ ,Ar) total hadronic cross section in LArIAT starts by selecting the pool of pion or kaon candidates and measuring their momentum. This is done through the series of selections on beamline and TPC information described in the next sections. The summary of the event selection in data is reported in Table 1.

0.1.1 Selection of Beamline Events

As shown in equation 5, we leverage the beamline particle identification and momentum measurement before entering the TPC as in input to evaluate the kinetic energy for the hadrons used in the cross sections measurements. Thus, we select the LArIAT data to keep only events whose wire chamber and time of flight information is registered (line 1 in in Table 1). Additionally, we perform a check of the plausibility of the trajectory inside the beamline detectors: given the position of the hits in the four wire chambers, we make sure the particle's trajectory does not cross any impenetrable material such as the collimator and the magnets steel (line 2 in in Table 1).

	Run-II Neg Pol	Run-II Pos Pol
1. Events Reconstructed in Beamline	158396	260810
2. Events with Plausible Trajectory	147468	240954
3. Beamline $\pi^-/\mu^-/e^-$ Candidate	138481	N.A.
4. Beamline K^+ Candidate	N.A	2837
5. Events Surviving Pile Up Filter	108929	2389
6. Events with WC2TPC Match	41757	1081
7. Events Surviving Shower Filter	40841	N.A.
8. Available Events For Cross Section	40841	1081

Table 1: Number of data events for Run-II Negative and Positive polarity

104 **0.1.2 Particle Identification in the Beamline**

105 In data, the main tool to establish the identity of the hadron of interest is the LArIAT
 106 tertiary beamline, in its function of mass spectrometer. We combine the measurement
 107 of the time of flight, TOF , and the beamline momentum, p_{Beam} , to reconstruct the
 108 invariant mass of the particles in the beamline, m_{Beam} , as follows

$$m_{Beam} = \frac{p_{Beam}}{c} \sqrt{\left(\frac{TOF * c}{l}\right)^2 - 1}, \quad (1)$$

109 where c is the speed of light and l is the length of the particle's trajectory between
 110 the time of flight paddels.

111 Figure 1 shows the mass distribution for the Run II negative polarity runs on the
 112 left and positive polarity runs on the right. We perform the classification of events
 113 into the different samples as follows:

- 114 • $\pi/\mu/e$: mass < 350 MeV
- 115 • kaon: 350 MeV < mass < 650 MeV
- 116 • proton: 650 MeV < mass < 3000 MeV.

117 Lines 3 and 4 in in Table 1 show the number of negative $\pi/\mu/e$ and positive K
 118 candidates which pass the mass selection for LArIAT Run-II data.

119 **0.1.3 TPC Selection: Halo Mitigation**

120 The secondary beam impinging on LArIAT secondary target produces a plethora of
 121 particles which propagates downstream. The presence of upstream and downstream
 122 collimators greatly abates the number of particles tracing down the LArIAT tertiary
 123 beamline. However, it is possible that more than one particle sneaks into the LArTPC
 124 during its readout time: the TPC readout is triggered by the particle firing the

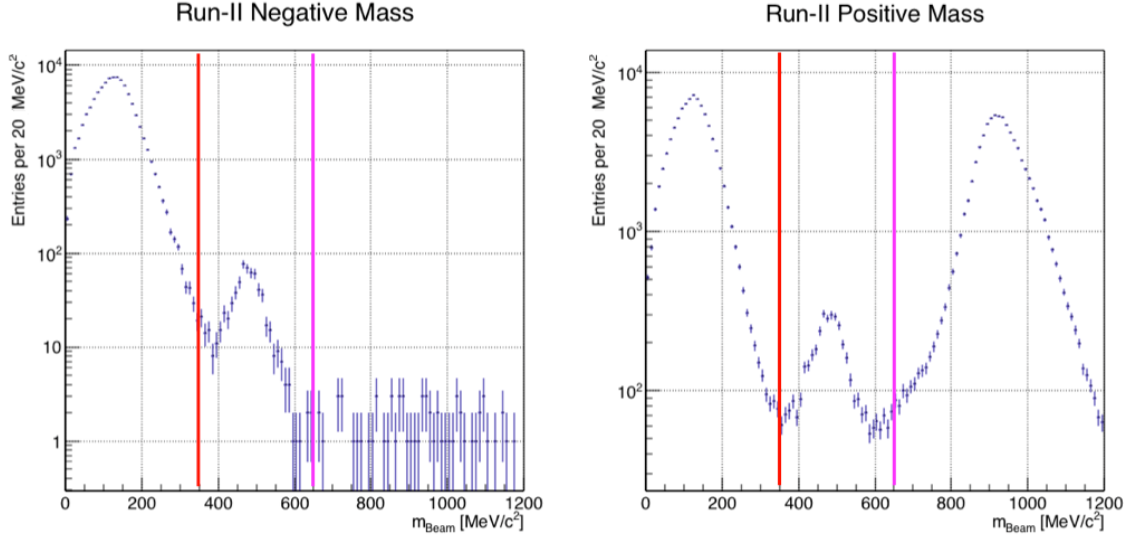


Figure 1: Distribution of the beamline mass as calculated according to equation 1 for the Run-II events reconstructed in the beamline, negative polarity runs on the left and positive polarity runs on the right. The classification of the events into $\pi^\pm/\mu^\pm/e^\pm$, K^\pm , or (anti)proton is based on these distributions, whose selection cut are represented by the vertical colored lines.

beamline detectors, but particles from the beam halo might be present in the TPC at the same time. We call “pile up” the additional traces in the TPC. We adjusted the primary beam intensity between LArIAT Run I and Run II to reduce the presence of events with high pile up particles in the data sample. For the cross section analyses, we remove events with more than 4 tracks in the first 14 cm upstream portion of the TPC from the sample (line 5 in in Table 1).

0.1.4 TPC Selection: Shower Removal

In the case of the (π^-, Ar) cross section, the resolution of beamline mass spectrometer is not sufficient to select a beam of pure pions. In fact, muons and electrons survive the selection on the beamline mass. It is important to notice that the composition of the negative polarity beam is mostly pions, as will be discussed in section 1.2.1. Still, we devise a selection on the TPC information to mitigate the presence of electrons

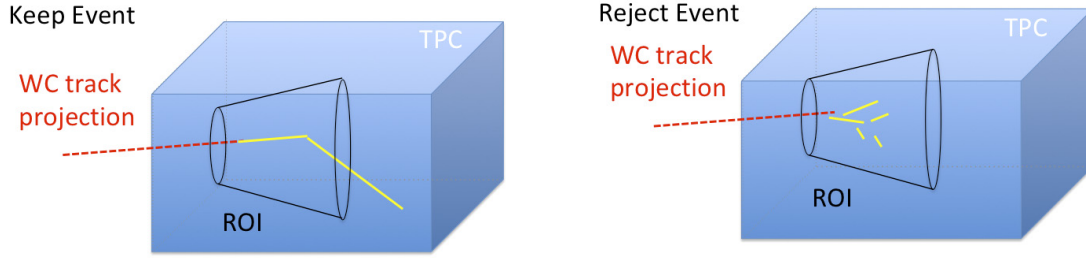


Figure 2: Visual rendering of the shower filter. The ROI is a cut cone, with a small radius of 4 cm, a big radius of 10 cm and an height of 42 cm (corresponding to 3 radiation lengths for electrons in Argon).

137 in the sample used for the pion cross section. The selection relies on the different
 138 topologies of a pion and an electron event in the argon: while the former will trace
 139 a track inside the TPC active volume, the latter will tend to “shower”, i.e. interact
 140 with the medium, producing bremsstrahlung photons which pair convert into several
 141 short tracks. In order to remove the shower topology, we create a region of interest
 142 (ROI) around the TPC track corresponding to the beamline particle. We look for
 143 short tracks contained in the ROI, as depicted in figure 4: if more then 5 tracks
 144 shorter than 10 cm are in the ROI, we reject the event. Line 7 in in Table 1 shows
 145 the number of events surviving this selection.

146 0.2 Beamline and TPC Handshake: the Wire Cham- 147 ber to TPC Match

148 For each event passing the selection on its beamline information, we need to identify
 149 the track inside the TPC corresponding to the particle which triggered the beamline
 150 detectors, a procedure we refer to as “WC to TPC match” (WC2TPC for short).
 151 In general, the TPC tracking algorithm will reconstruct more than one track in the
 152 event, partially due to the fact that hadrons interact in the chamber and partially
 153 because of pile up particles during the triggered TPC readout time, as shown in

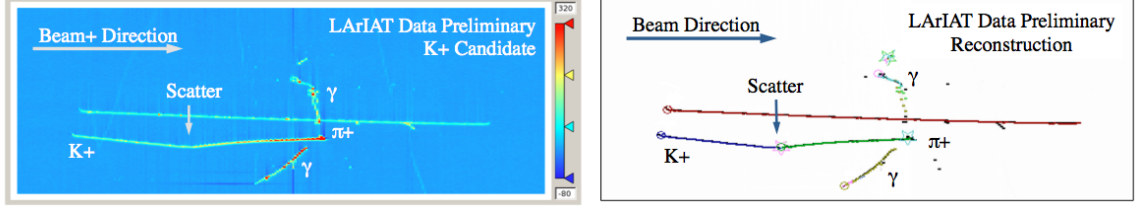


Figure 3: Kaon candidate event: on the right, event display showing raw quantities; on the left, event display showing reconstructed tracks. In the reconstructed event display, different colors represent different track objects. A kink is visible in the kaon ionization, signature of a hadronic interaction: the tracking correctly stops at the kink position and two tracks are formed. An additional pile-up track is so present in the event (top track in red).

figure 3.

We attempt to uniquely match one wire chamber track to one and only one reconstructed TPC track. In order to determine if a match is present, we apply a geometrical selection on the relative the position of the wire chamber and TPC tracks. We start by considering only TPC tracks whose first point is in the first 2 cm upstream portion of the TPC for the match. We project the wire chamber track to the TPC front face where we define the coordinates of the projected point as x_{FF} and y_{FF} . For each considered TPC track, we define ΔX as the difference between the x position of the most upstream point of the TPC track and x_{FF} . ΔY is defined analogously. We define the radius difference, ΔR , as $\Delta R = \sqrt{\Delta X^2 + \Delta Y^2}$. We define as α the angle between the incident WC track and the TPC track in the plane that contains them. If $\Delta R < 4$ cm, $\alpha < 8^\circ$, a match between WC-track and TPC track is found. We describe how we determine the value for the radius and angular selection in Section 1.5.1. We discard events with multiple WC2TPC matches. We use only those TPC tracks that are matched to WC tracks in the cross section calculation. Line 6 in Table 1 shows the number of events where a unique WC2TPC match was found.

In MC, we mimic the matching between the WC and the TPC track by constructing a fake WC track using truth information at wire chamber four. We then apply the same WC to TPC matching algorithm as in data.

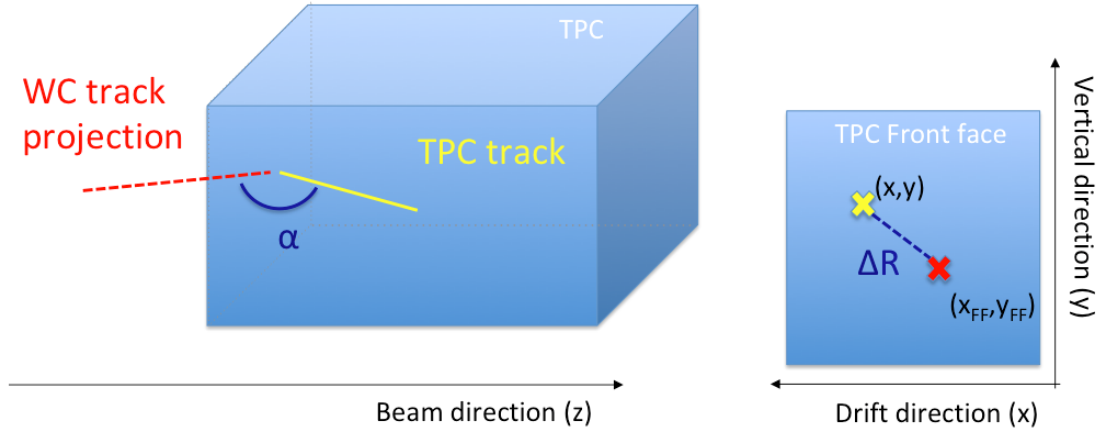


Figure 4: Visual rendering of the wire chamber to TPC match.

0.3 The Thin Slice Method

Once we have selected the pool of hadron candidates and we have identified the TPC track corresponding to the beamline event, we apply the thin slice method to measure the cross section, as the following sections describe.

0.3.1 Cross Sections on Thin Target

Cross section measurements on a thin target have been the bread and butter of nuclear and particle experimentalists since the Geiger-Marsden experiments [29]. At their core, this type of experiments consists in shooting a beam of particles with a known flux on a thin slab of material and recording the outgoing flux.

In general, the target is not a single particle, but rather a slab of material containing many diffusion centers. The so-called “thin target” approximation assumes that the target centers are uniformly distributed in the material and that the target is thin compared to the projectile interaction length, so that no center of interaction sits in front of another. In this approximation, the ratio between the number of particles interacting in the target N_{Int} and number of incident particles N_{Inc} on the target determines the interaction probability $P_{\text{Interacting}}$, which is the complementary to one

189 of the survival probability $P_{Survival}$. Equation 2

$$P_{Survival} = 1 - P_{Interacting} = 1 - \frac{N_{Int}}{N_{Inc}} = e^{-\sigma_{TOT}n\delta X} \quad (2)$$

190 describes the probability for a particle to survive the thin target. This formula relates
 191 the interaction probability to the total hadronic cross section (σ_{TOT}), the density of
 192 the target centers (n)¹ and the thickness of the target along the incident hadron
 193 direction (δX). If the target is thin compared to the interaction length of the process
 194 considered, we can Taylor expand the exponential function in equation 2 and find
 195 a simple proportionality relationship between the cross section and the number of
 196 incident and interacting particles, as shown in equation 3:

$$1 - \frac{N_{Int}}{N_{Inc}} = 1 - \sigma_{TOT}n\delta X + O(\delta X^2). \quad (3)$$

197 Solving for the cross section, we find:

$$\sigma_{TOT} = \frac{1}{n\delta X} \frac{N_{Int}}{N_{Inc}}. \quad (4)$$

198 **0.3.2 Not-so-Thin Target: Slicing the Argon**

199 The interaction length of pions and kaons in argon is expected to be of the order
 200 of 50 cm for pions and 100 cm for kaons. Thus, the LArIAT TPC, with its 90 cm
 201 of length, is not a thin target. However, the fine-grained tracking of the LArIAT
 202 LArTPC allows us to treat the argon volume as a sequence of many adjacent thin
 203 targets.

204 As described in Chapter ??, LArIAT wire planes consist of 240 wires each. The
 205 wires are oriented at +/- 60° from the vertical direction at 4 mm spacing, while the

1. The scattering center density in the target, n , relates to the argon density ρ , the Avogadro number N_A and the argon molar mass m_A as $n = \frac{\rho N_A}{m_A}$.

beam direction is oriented 3 degrees off the z axis in the XZ plane. The wires collect signals proportional to the energy loss of the hadron along its path in a $\delta X = 4$ mm/ $(\sin(60^\circ)\cos(3^\circ)) \approx 4.7$ mm slab of liquid argon. Thus, one can think to slice the TPC into many thin targets of $\delta X = 4.7$ mm thickness along the direction of the incident particle, making a measurement at each wire along the path.

Considering each slice j a “thin target”, we can apply the cross section calculation from Equation 2.1 iteratively, evaluating the kinetic energy of the hadron as it enters each slice, E_j^{kin} . For each WC2TPC matched particle, the energy of the hadron entering the TPC is known thanks to the momentum and mass determination by the tertiary beamline,

$$E_{FrontFace}^{kin} = \sqrt{p_{Beam}^2 - m_{Beam}^2} - m_{Beam} - E_{loss}, \quad (5)$$

where E_{loss} is a correction for the energy loss in the uninstrumented material between the beamline and the TPC front face. The energy of the hadron at each slab is determined by subtracting the energy released by the particle in the previous slabs. For example, at the j^{th} point of a track, the kinetic energy will be

$$E_j^{kin} = E_{FrontFace}^{kin} - \sum_{i < j} E_{Dep,i}, \quad (6)$$

where $E_{Dep,i}$ is the energy deposited at each argon slice before the j^{th} point as measured by the calorimetry associated with the tracking.

If the particle enters a slice, it contributes to $N_{Inc}(E^{kin})$ in the energy bin corresponding to its kinetic energy in that slice. If it interacts in the slice, it also contributes to $N_{Int}(E^{kin})$ in the appropriate energy bin. The cross section as a function of kinetic energy, $\sigma_{TOT}(E^{kin})$ will then be proportional to the ratio $\frac{N_{Int}(E^{kin})}{N_{Inc}(E^{kin})}$.

Our goal is to measure the total interaction cross section, independently from the topology of the interaction. Thus, we determine that a hadron interacted simply by

	min	max
X	1 cm	46 cm
Y	-15 cm	15 cm
Z	0 cm	86 cm

Table 2: Fiducial volume boundaries used to determine cross section interaction point.

228 requiring that the last point of the WC2TPC matched track lies inside the fiducial
 229 volume, whose boundaries are defined in Table 2. If the TPC track stops within the
 230 fiducial volume, its last point will be the interaction point; if the track crosses the
 231 boundaries of the fiducial volume, the track will be considered “through going” and
 232 no interaction point will be found. The only slabs considered to fill the N_{Inc} and
 233 N_{Inc} plots are the slabs included the fiducial volume.

234 0.3.3 Corrections to the Raw Cross Section

235 Equation 2.1 is a prescription for measuring the cross section in case of a pure beam
 236 of the hadron of interest and 100% efficiency in the determination of the interaction
 237 point. For example, if LArIAT had a beam of pure pions and were 100% efficient
 238 in determining the interaction point within the TPC, the pion cross section in each
 239 energy bin would be given by

$$\sigma_{TOT}^{\pi^-}(E_i) = \frac{1}{n\delta X} \frac{N_{\text{Int}}^{\pi^-}(E_i)}{N_{\text{Inc}}^{\pi^-}(E_i)}. \quad (7)$$

240 Unfortunately, this is not the case. In fact, the selection used to isolate pions
 241 in the LArIAT beam allows for the presence of some muons and electrons as back-
 242 ground. Also, the LArIAT TPC is not 100% efficient in determining the interaction
 243 point. Therefore we need to apply two corrections evaluated on the MC in order to
 244 extract the true cross section from LArIAT data: the background subtraction and
 245 the efficiency correction. Still using the pion case as example, we estimate the pion

246 cross section in each energy bin changing Equation 7 into

$$\sigma_{TOT}^{\pi^-}(E_i) = \frac{1}{n\delta X} \frac{N_{\text{Int}}^{\pi^-}(E_i)}{N_{\text{Inc}}^{\pi^-}(E_i)} = \frac{1}{n\delta X} \frac{\epsilon^{\text{Inc}}(E_i)[N_{\text{Int}}^{\text{TOT}}(E_i) - B_{\text{Int}}(E_i)]}{\epsilon^{\text{Int}}(E_i)[N_{\text{Inc}}^{\text{TOT}}(E_i) - B_{\text{Inc}}(E_i)]}, \quad (8)$$

247 where $N_{\text{Int}}^{\text{TOT}}(E_i)$ and $N_{\text{Incident}}^{\text{TOT}}(E_i)$ is the measured content of the interacting and
 248 incident histograms for events that pass the event selection, $B_{\text{Int}}(E_i)$ and $B_{\text{Inc}}(E_i)$
 249 represent the contributions from beamline background to the interacting and incident
 250 histograms respectively, and $\epsilon^{\text{Int}}(E_i)$ and $\epsilon^{\text{Inc}}(E_i)$ are the efficiency corrections for said
 251 histograms.

252 As we will show in section 2.2.2, the background subtraction for the interacting
 253 and incident histograms can be translated into a corresponding relative pion content
 254 $C_{\text{Interacting}}^{\pi MC}(E_i)$ and $C_{\text{Incident}}^{\pi MC}(E_i)$ and the cross section re-written as follows

$$\sigma_{TOT}^{\pi^-}(E_i) = \frac{1}{n\delta X} \frac{\epsilon^{\text{Inc}}(E_i)}{\epsilon^{\text{Int}}(E_i)} \frac{C_{\text{Int}}^{\pi MC}(E_i)}{C_{\text{Inc}}^{\pi MC}(E_i)} \frac{N_{\text{Int}}^{\text{TOT}}(E_i)}{N_{\text{Inc}}^{\text{TOT}}(E_i)}. \quad (9)$$

255 0.4 Procedure testing with truth quantities

256 The (π^-, Ar) and (K^+, Ar) total hadronic cross section implemented in Geant4 can be
 257 used as a tool to validate the measurement methodology. We describe here a closure
 258 test done on Monte Carlo to prove that the methodology of slicing the TPC retrieves
 259 the underlying cross section distribution implemented in Geant4 within the statistical
 260 uncertainty.

261 For pions and kaons in the considered energy range, the Geant4 inelastic model
 262 adopted is “BertiniCascade”; the pion elastic cross sections are modeled on Chips,
 263 while the kaon elastic cross sections are modeled on Gheisha and Chips.

264 For the validation test, we fire a sample of pions and a sample of kaons inside
 265 the LArIAT TPC active volume using the Data Driven Monte Carlo (see section
 266 1.2.2). We apply the thin-sliced method using only true quantities to calculate the

267 hadron kinetic energy at each slab in order to decouple reconstruction effects from
 268 possible issues with the methodology. For each slab of 4.7 mm length along the
 269 path of the hadron, we integrate the true energy deposition as given by the Geant4
 270 transportation model. Then, we recursively subtracted it from the hadron kinetic
 271 energy at the TPC front face to evaluate the kinetic energy at each slab until the
 272 true interaction point is reached. Since the MC is a pure beam of the hadron of
 273 interest and truth information is used to retrieve the interaction point, no correction
 274 is applied. Doing so, we obtain the true interacting and incident distributions for
 275 the considered hadron and we obtain the true MC cross section as a function of the
 276 hadron true kinetic energy.

277 Figure 5 shows the total hadronic cross section for argon implemented in Geant4
 278 10.03.p1 (solid lines) overlaid with the true MC cross section as obtained with the
 279 sliced TPC method (markers) for pions on the left and kaons on the right; the total
 280 cross section is shown in green, the elastic cross section in blue and the inelastic
 281 cross section in red. The nice agreement with the Geant4 distribution and the cross
 282 section obtained with the sliced TPC method gives us confidence in the validity of
 283 the methodology.

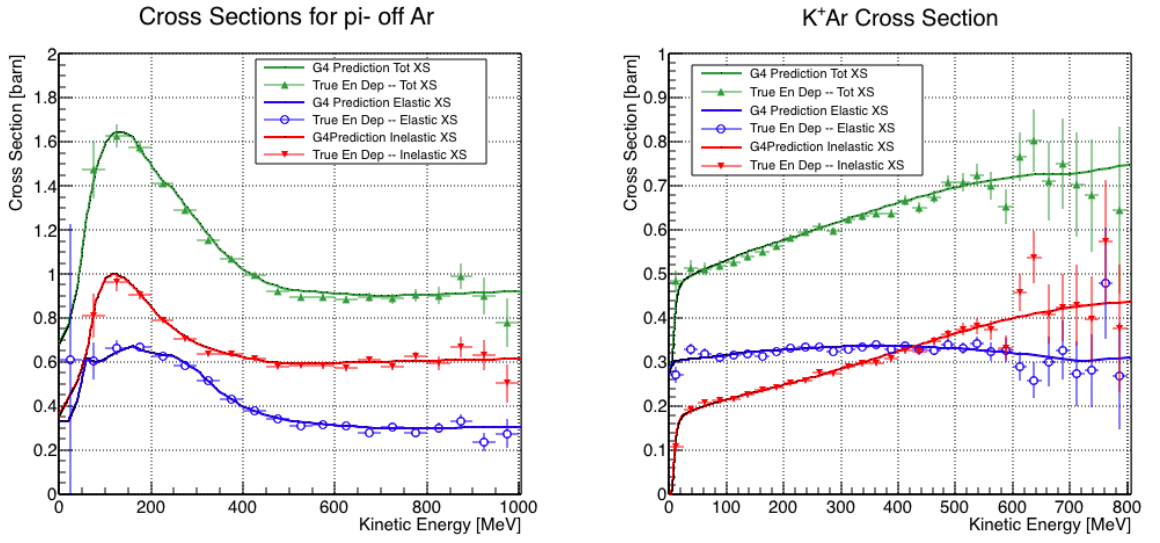


Figure 5: Hadronic cross sections for (π^-, Ar) on the left and (K^+, Ar) on the right as implemented in Geant4 10.03.p1 (solid lines) overlaid the true MC cross section as obtained with the sliced TPC method (markers). The total cross section is shown in green, the elastic cross section in blue and the inelastic cross section in red.

Chapter 1

Data and MC preparation for the Cross Section Measurements

This chapter describes the preparatory work done on the the data and Monte Carlo samples used for the cross section analyses. This entails the choice of the datasets and the production of the information needed to construct the Monte Carlo Simulation (section 1.1), the construction and use of said Monte Carlo simulation (section 1.2), the study and optimization of the tracking in the TPC for the cross section analyses (section 1.5), the calibration of the calorimetry response and related energy studies (section 1.6).

1.1 Cross Section Analyses Data Sets

We choose LArIAT Run-II as the data period for the (π^-, Ar) and (K^+, Ar) total hadronic cross section analyses. Data taking for the this period started on 03/15/2016 and ended on 07/31/2016. Since we are interested in beamline and TPC information, we ask basic requirements on the operational status of the time of fight, wire chambers and TPC to form the good run list for this period, which we informally call “lovely runs”.

301 The subset of lovely runs chosen for the (π^-, Ar) total hadronic cross section
 302 analysis includes only the -60A and -100A magnet configurations in negative polarity,
 303 even if LArIAT explored several other beamline configurations during Run-II. The
 304 -60A and -100A combined data set accounts for approximately 90% of the total Run-
 305 II negative polarity runs. The choice of the main two beamline settings limits the
 306 need for the production of many MC sets and related corrections, still maintaining a
 307 high number of events.

308 Similarly, the subset of lovely runs chosen for the (K^+, Ar) total hadronic cross
 309 section analysis includes only the +60A and +100A magnet configurations in positive
 310 polarity. It should be noted that kaons are extremely rare in the +60A sample, thus
 311 the data sample for the (K^+, Ar) cross section after the mass selection is about 90%
 312 +100A runs, as shown in Table 1.1.

313 For the first measurements in LArIAT that uses both beamline and TPC infor-
 314 mation, we choose strict requirements on the reconstruction of the WC tracks, the
 315 so-called “Picky Track” sample (see Section ??). This choice presents two advantages:
 316 the uncertainty on the momentum reconstruction for the “Picky Tracks” sample is
 317 smaller compared to the “High Yield” sample, and the comparison with the beam-
 318 line MC results is straightforward. A possible future update and cross check of these
 319 analysis would be the use of the High Yield sample, where the statistics is about three
 320 times higher.

321 The breakdown of beamline events as a function of the magnets settings is shown
 322 in Table 1.1. The choice of the data sets determines the production of beamline MC
 323 and serves as basis for the production of Data Driven MC, as shown in the next
 324 sections.

1.2 Construction of a Monte Carlo Simulation for LArIAT

For the simulation of LArIAT events and for the simulation of the datasets' particle make up, we use a combination of two MC generators: the G4Beamline Monte Carlo and the Data Driven single particle Monte Carlo (DDMC). We use the G4Beamline MC to simulate the particle transportation in the beamline and calculate the particle composition of the beam just after the fourth Wire Chamber (WC4). In order to simulate the beamline particles after WC4 and in the TPC, we use the DDMC.

1.2.1 G4Beamline

G4Beamline simulates the beam collision with the LArIAT secondary target, the energy deposited by the particles in the LArIAT beamline detectors, and the action of the LArIAT magnets, effectively accounting for particle transportation through the beamline from the LArIAT target until “Big Disk”, a fictional, void detector located just before the LArIAT cryostat. At the moment of this writing, G4Beamline does not simulated the responses of the beamline detectors. It is possible to interrogate the truth level information of the simulated particles in several points of the geometry. In order to ease the handshake between G4Beamline and the DDMC, we ask for the beam composition just after WC4. Since LArIAT data are taken under different beam conditions, we need to simulate separately the beam composition according to the magnets' settings and the secondary beam intensity with G4Beamline. For the

	I = 60 A	I = 100 A	Total
Data Events after $\pi/\mu/e$ Mass Selection	67068	71413	138481
Data Events after K Mass Selection	274	2563	2837

Table 1.1: Number of data events which fit the $\pi/\mu/e$ or K mass hypothesis as a function of magnet settings.

pion cross section analysis the relevant beam conditions are secondary beam energy of 64 GeV, negative polarity magnet with current of 100 A and 60 A. For the kaon cross section analysis the relevant beam conditions is a secondary beam energy of 64 GeV, positive polarity magnet with current of 100 A.

Beam Composition for Negative Pion Cross Section

Even if pions are by far the biggest beam component in negative polarity runs, the LArIAT tertiary beam is not a pure pion beam. While useful to discriminate between pions, kaons, and protons, the beamline detectors are not sensitive enough to discriminate among the lighter particles in the beam: electrons, muons and pions fall under the same mass hypothesis. Thus, we need to assess the contamination from beamline particles other than pions in the event selections used for the pion cross section analysis and correct for its effects. The first step of this process is assessing the percentage of electrons and muons in the $\pi/\mu/e$ beamline candidates via the G4Beamline MC. Since the beamline composition is a function of the magnet settings, we simulate separately events for magnet current of -60A and -100A. Figure 2.4 shows the momentum predictions from G4Beamline overlaid with data for the 60A runs (left) and for the 100A runs (right). The predictions for electrons, muons and pions have been staggered and their sum is area normalized to data. Albeit not perfect, these plots show a reasonable agreement between the momentum shapes in data and MC. We attribute the difference in shape to the lack of simulation of the WC efficiency in the MC which is momentum dependent and leads to enhance the number events in the center of the momentum distribution.

Table 2.1 shows the beam composition per magnet setting after the mass selection according to the G4Beamline simulation.

The estimated beam composition is used as a basis to estimate the background contamination in the (π^-, Ar) cross section measurement, whose full treatment is

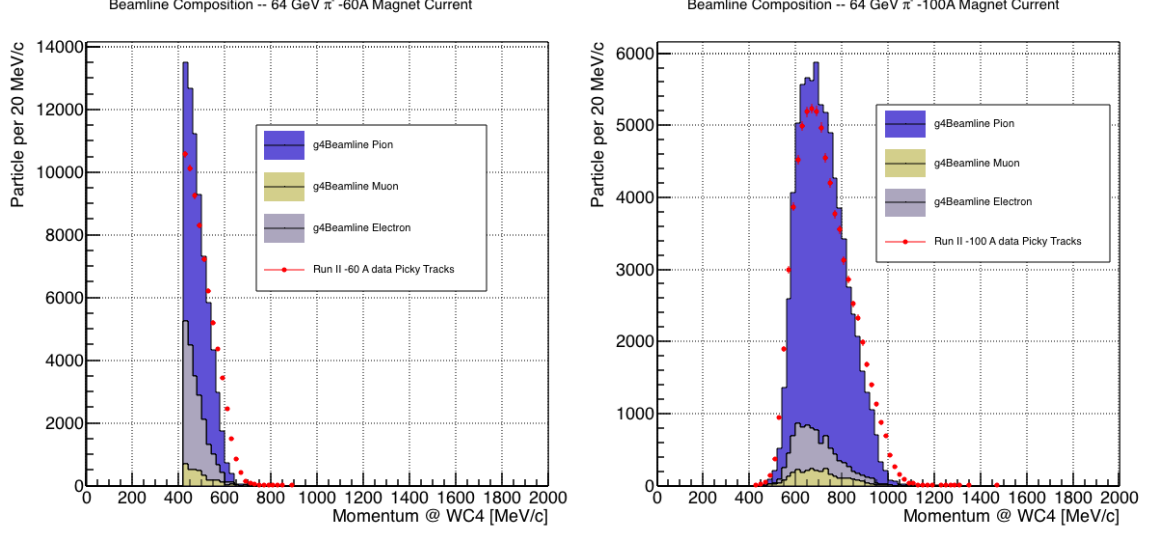


Figure 1.1: Beam composition for the -60A runs (left) and -100A runs (right). The solid blue plot represents the simulated pion content, the yellow plot represents the simulated muon content and the grey plot represents the simulated electron content. The plots are area normalized to the number of data events, shown in red.

	I = -60 A	I = -100 A
G4Pions	68.8 %	87.4 %
G4Muons	4.6 %	3.7 %
G4Electrons	26.6 %	8.9 %

Table 1.2: Simulated beamline composition per magnet settings

371 described in section 1.3.

372 **Beam Composition for Positive Kaon Cross Section**

373 In the positive polarity runs, the tertiary beam composition is mainly pions and
374 protons. The left side of Figure 1.2 shows the predictions for the momentum spectra
375 for the 100A positive runs according to G4Beamline (solid colors) overlaid with data
376 (black points). Since the LArIAT beamline detectors can discriminate between kaons
377 and other particles, we do not rely on the G4Beamline simulation to estimate the
378 beamline contamination in the pool of kaon candidates (as in the case of the pion
379 cross section), but rather we use a data drive approach. The basic idea of this data
380 driven approach is to estimate the bleed over from high and low mass peaks under the
381 kaon peak by fitting the tails of the $\pi/\mu/e$ and proton mass distributions, as shown
382 in Figure 1.2 right side. Since the shape of the tails is unknown, the estimate is done
383 multiple times varying the range and shape for reasonable functions. For example, to
384 estimate the proton content under the kaon peak, we start by fitting the left tail of
385 the proton mass distribution with a gaussian function between $650 \text{ MeV}/c^2$ and 750
386 MeV/c^2 . We extend the fit function under the kaon peak and integrate the extended
387 fit function between $350\text{-}650 \text{ MeV}/c^2$. We integrate the mass histogram in the same
388 range and calculate the proton contamination as the ratio between the two integrals.
389 We repeat this procedure for several fit shapes (gaussian, linear and exponential
390 functions) and tail ranges. Finally, we calculate the contamination as the weighted
391 average of single estimates, where the weights are calculated to be the $1./\chi^2$ of the
392 tail fits. The procedure is repeated for lighter particles mass peak independently.
393 With 12 iterations of this method we find a proton contamination of $0.2 \pm 0.5 \%$
394 and a contamination from the lighter particles of $5 \pm 2 \%$. The estimate of the
395 proton background is currently not used in the kaon cross section analysis, but it is
396 a fundamental step to retrieve the true kaon cross section which will be implemented

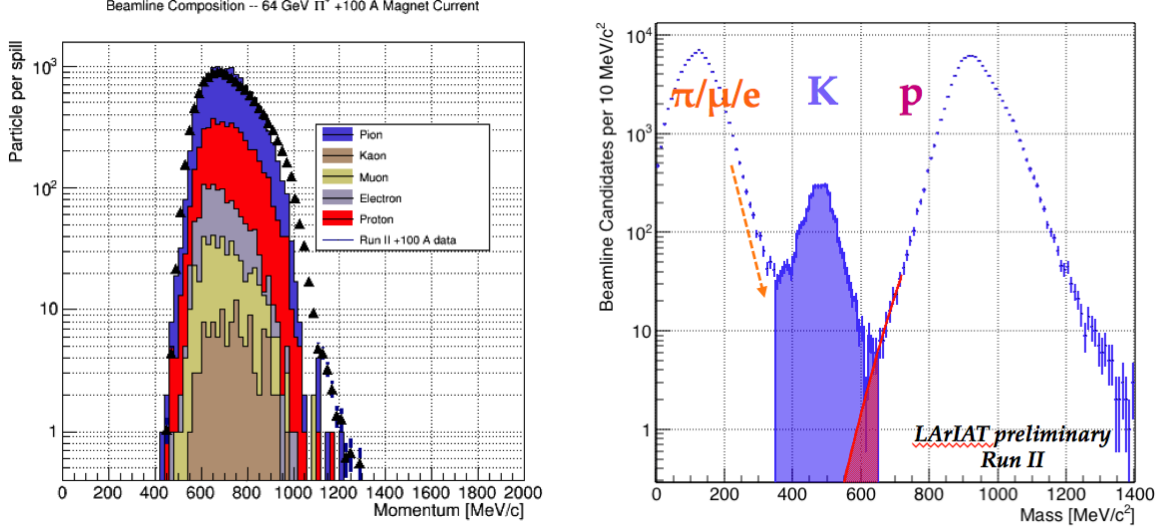


Figure 1.2: *Left*: Beam composition for the +100A runs after WC4 (no mass selection applied). The solid colors represent the contributions from the G4Beamline simulated particles: blue plot represents the simulated pion content, the yellow plot represents the simulated muon content and the grey plot represents the simulated positron content, the red the proton content and the mustard the kaon content. The plots are area normalized to the number of data events, shown in black. *Right*: Mass distribution for the Run-II positive runs, where the area under the kaon mass peak is highlighted in purple. The area under the extension of a possible fit for the proton tail is highlighted in red.

in the analysis next step.

1.2.2 Data Driven MC

The Data Driven single particle Monte Carlo (DDMC) is a single particle gun which simulates the particle transportation from WC4 into the TPC leveraging on the beamline data information. The DDMC uses the data momentum and position at WC4 to derive the event generation: a general sketch of the DDMC workflow is shown in Figure 1.3.

When producing a DDMC sample, beamline data from a particular running period and/or running condition are selected first. For example, data for the negative 60A runs and for the negative 100A runs inform the event generation stage of two different DDMC samples. Figure 1.4 schematically shows the data quantities of in-

408 terest leveraged from data: the momentum (P_x, P_y, P_z) and position (X, Y) at WC4.
 409 For each data event, we obtain the particle position (X, Y) at WC4 directly from the
 410 data measurement; we calculate the components of the momentum using the beamline
 411 measurement of the momentum magnitude in conjunction with the hits on WC3 and
 412 WC4 to determine the direction of the momentum vector, as described in section ??.
 413 The momentum and position of the selected data form a 5-dimensional tupla, which
 414 we sample thousands of times through a 5-dimensional hit-or-miss sampling proce-
 415 dure to generate the MC events. This generates MC events with the same momentum
 416 and position distributions as data, with the additional benefit of accounting for the
 417 correlations between the P_x, P_y, P_z, X, Y variables. As an example, the results of the
 418 DDMC generation compared to data for the kaon +100A sample are shown in figure
 419 1.5 for the P_z, X and Y distributions; as expected, MC and data agree within the
 420 statistical uncertainty by construction. A LArSoft simulation module then launches
 421 single particle MC from $z = -100$ cm (the location of the WC4) using the MC gener-
 422 ated events. The particles are free to decay and interact in their path from WC4 to
 423 the TPC according to the Geant4 simulation.

424 Using the DDMC technique ensures that the MC and data particles have very
 425 similar momentum, position and angular distributions at WC4 and allows us to use
 426 the MC sample in several occasions: to calibrate the energy loss upstream of the TPC
 427 (see Section 1.4), to estimate the background contamination to the pion cross section
 428 (see Section 1.3), or to study the tracking and the calorimetric performance (sections
 429 1.5 and 1.6). A small caveat is in order here: the DDMC is a single particle Monte
 430 Carlo, which means that the beam pile-up is not simulated.

431 Six samples are the basis for the MC used in the pion cross section measurement:
 432 three samples of ~ 340000 pions, muons and electrons to simulate the negative 60A
 433 runs, and three samples of ~ 340000 pions, muons and electrons for the negative 100A
 434 runs.

435

The MC used for the kaon cross section analysis is a sample of **NUMBERS** kaons.

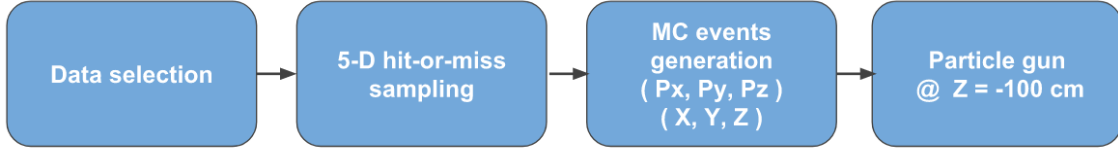


Figure 1.3: Workflow for Data Driven single particle Monte Carlo production.

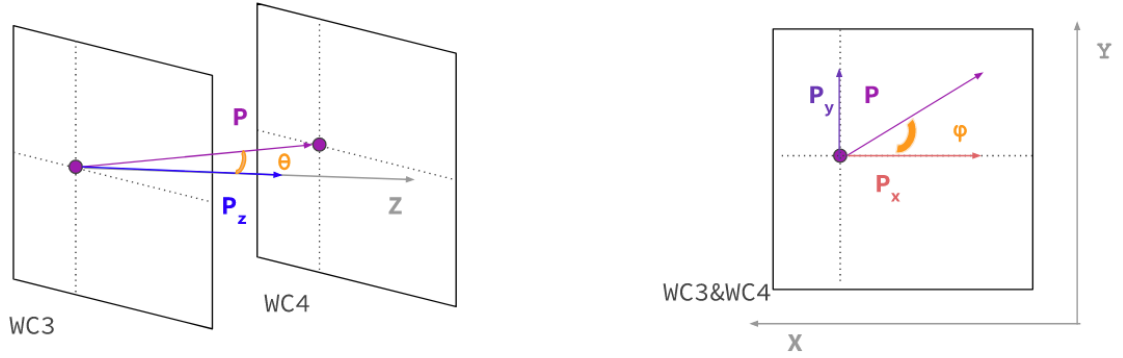


Figure 1.4: Scheme of the quantities of interest for the DDMC event generation: P_x, P_y, P_z, X, Y at WC4.

436

1.3 Estimate of Backgrounds in the Pion Cross

437

Section

438

We use the beamline simulation and the DDMC simulation to estimate the back-

439

ground in the total hadronic pion cross section. Two categories of background exists

440

for the negative pion cross section measurement: the one related to the pion interac-

441

tion in the chamber, discussed in Section 1.3.1 and the one related to the beamline

442

contamination, discussed in Section 1.3.2.

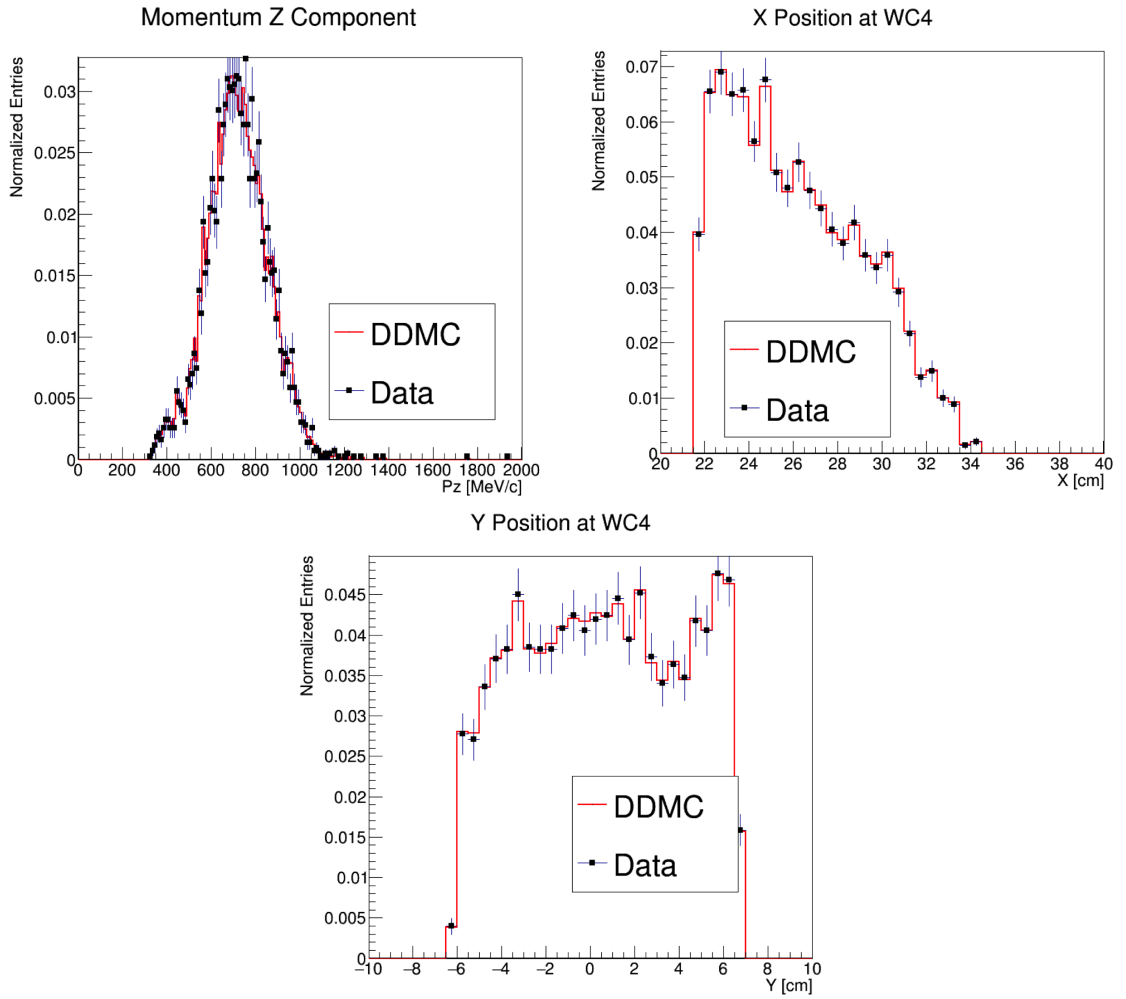


Figure 1.5: Comparison between generated quantities and data distributions for the 100A kaon sample: Z component of the momentum at WC4 (top left), X position at Wire Chamber 4 (top right), Y position at Wire Chamber 4 (bottom).

1.3.1 Background from Pion Capture and Decay

Our goal is to measure the total hadronic cross section for negative pions in argon. Since pion capture can be classified as an electromagnetic process and pion decay is a weak process, capture and decay represent unwanted interactions. We present here a study of capture and decay in Monte Carlo and the solution we adopted to mitigate their occurrence in the data sample.

For this MC study, we use a sample of MC pions generated according to the -60A beam profile with the DDMC (see Section 1.2.2). It is important to notice that capture occurs predominantly at rest, while decay may occur both in flight and at rest. Thus, we can highly mitigate capture and decay at rest by removing pions which would release all their energy in the TPC and stop. This translates into a momentum selection, where we keep only events whose WC momentum is above a certain threshold. Figure 1.6 shows the true momentum distribution for the primary pions¹ that arrive to the TPC (pink), that capture (green) or decay (blue) inside the TPC, on a linear and log scale vertical axis.

In order to choose the selection value for the wire chamber momentum, it is beneficial to estimate the ratio of events which capture or decay that survive the selection in MC as a function of the momentum threshold, and compare it with the survival ratio for all events. This is done in figure 1.7. We define the survival ratio simply as the number of events surviving the true momentum selection divided by the number of events of that category. We calculate the survival ratio separately for the three event categories explained above: total (pink), capture (green) and decay (blue). Selecting pions with momentum greater than $420\text{ MeV}/c$ reduces the capture events by 99% while maintaining about 80% of the total data sample. Figure 1.8

1. We use here the Geant4 denomination “primary” to indicate that the pion considered does not undergo interactions modifying its energy before getting to the TPC. In fact, not every pion shot from wire chamber four will arrive to the TPC as primary, some will decay or interact before the TPC.

467 shows the ratio of events which end their life in capture (green) or decay (blue) over
468 the total number of events as a function of the true momentum at wire chamber
469 four. This ratio is slightly dependent on the inelastic cross section implemented in
470 Geant4, as we are able to register a pion capture (or decay) only if it did not interact
471 inelastically in the TPC. We choose a momentum threshold of 420 MeV/c because the
472 percentage of capture events drops below 1% and the percentage of decays is never
473 above 2% for momenta greater than 420 MeV/c. After the momentum selection, we
474 evaluate the contribution of capture and decay to be a negligibly small background to
475 the cross section measurement compared to the background related to the beamline.

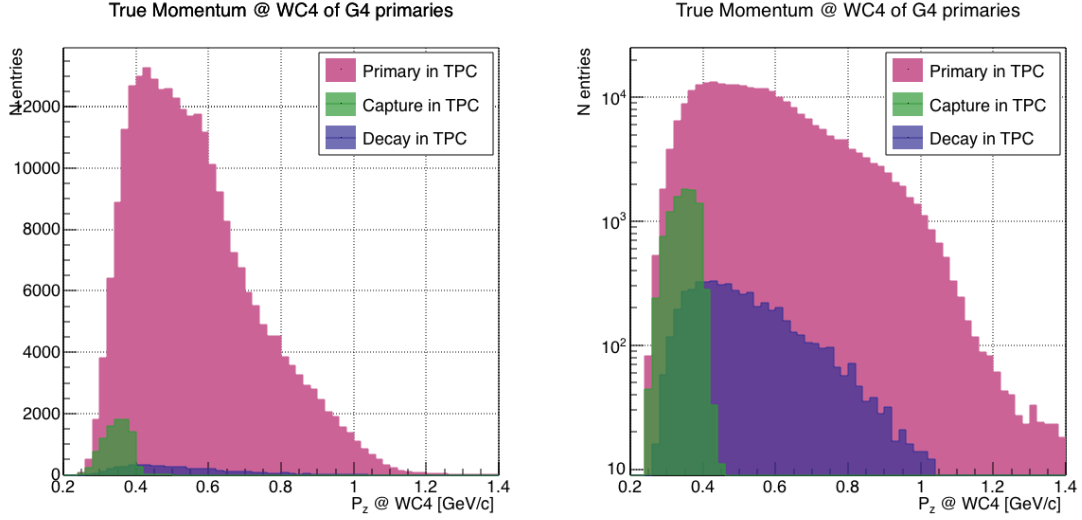


Figure 1.6: True momentum distribution at wire chamber 4 for every simulated pion arriving in the TPC (pink), ending its life in capture (green) or in decay (blue) in the TPC, linear vertical axis on the left, logarithmic on the right.

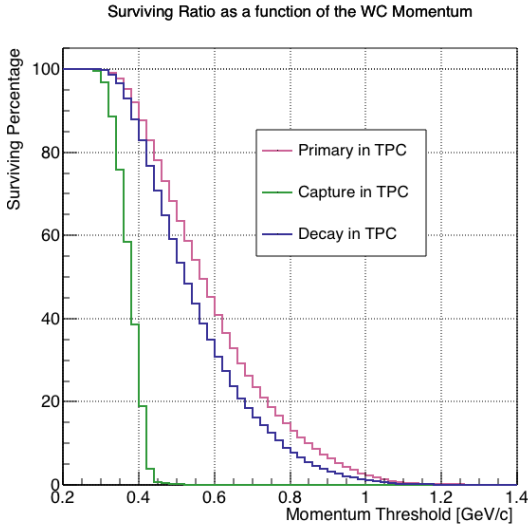


Figure 1.7: Survival ratio as a function of selection threshold on true momentum at wire chamber four for every simulated pion arriving in the TPC (pink), capture (green) or in decay (blue).

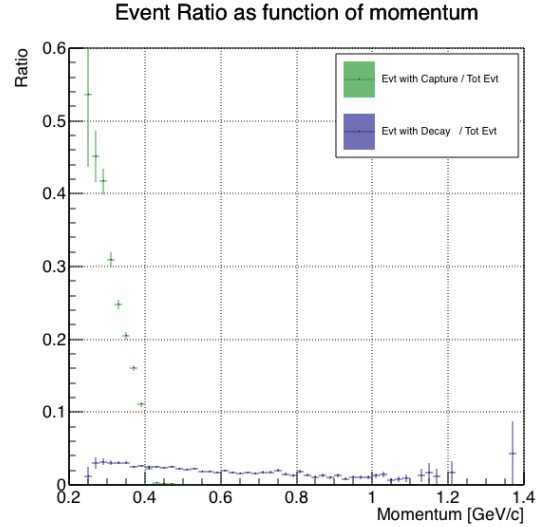


Figure 1.8: Ratio between the capture (green) and decay (blue) events over the total number of events as a function of the true momentum at wire chamber four.

	Magnet Current -60A			Magnet Current -100 A		
	MC π^-	MC μ^-	MC e^-	MC π^-	MC μ^-	MC e^-
Total Initial events	334500	334500	334500	344500	344500	344500
After Multiplicity Rejection	330668	333420	198065	326576	344208	201380
After WC2TPC Selection	218239	296333	91139	230418	300228	98834
Evts After Shower Rejection	208063	288914	20293	219882	293585	17780
Selection Survival Rate	62.3%	86.6%	6.1%	63.8%	85.5%	5.2%
Beam Composition @WC4	68.8%	4.6 %	26.6 %	87.4 %	3.7 %	8.9 %
Beam Composition @TPC FF	88.5%	8.2%	3.3 %	94.0%	5.3%	0.7%

Table 1.3: MC selection flow per particle species.

1.3.2 Beamline Background

As shown in Section 1.2.1, we use G4Beamline to estimate the beam composition at WC4, obtaining the composition shown in Table 2.1. The next step to estimate the beamline background in the cross section measurement is propagating pions, muons and electrons to the TPC and evaluate their contribution to the cross section. To do so, we simulate the same number of electrons, muons and pions with the DDMC and we apply the same selection filters on the three samples. The number of events per particle species surviving this selection is shown on table 1.3.

In order to reproduce the closest make up of the beam to data, we weight each event of a given particle species according to the estimated beam composition. In case of 60A runs, for example, the weights are 0.688 for pions, 0.046 for muons and 0.266 for electrons. We produce accordingly the interacting and incident histograms for the events surviving the selection, staggering the contributions for each particle species, as shown in Figure 1.9. From those histograms, we are able to evaluate the relative contribution of pions and background to each bin of the interacting and incident histograms separately and obtain the respective corrections for data. We take here the interacting histogram as example, noting that the derivation of the

493 correction for the incident histogram is identical. The number of entries in each bin
 494 of the interacting plot (Figure 1.9 left) is $N_{\text{Interacting}}^{\text{TOT}}(E_i)$, equal to the sum of the pions
 495 and background in that bin, namely

$$N_{\text{Interacting}}^{\text{TOT}}(E_i) = N_{\text{Interacting}}^{\pi}(E_i) + \underbrace{N_{\text{Interacting}}^{\mu}(E_i) + N_{\text{Interacting}}^e(E_i) + N_{\text{Interacting}}^{\text{Secondary}}(E_i)}_{B_{\text{Interacting}}(E_i)}. \quad (1.1)$$

496 Thus, the relative contribution of pions to each bin in MC can be calculated as follows

$$C_{\text{Interacting}}^{\pi MC}(E_i) = \frac{N_{\text{Interacting}}^{\pi MC}(E_i)}{N_{\text{Interacting}}^{\text{TOTMC}}(E_i)} = \frac{N_{\text{Interacting}}^{\text{TOTMC}}(E_i) - B_{\text{Interacting}}^{\text{MC}}(E_i)}{N_{\text{Interacting}}^{\text{TOTMC}}(E_i)}. \quad (1.2)$$

497 In order to evaluate the pion content of each bin in data, we scale the measured
 498 bin content by the corresponding pion contribution found in MC, as follows

$$N_{\text{Interacting}}^{\pi \text{RecoData}} = N_{\text{Interacting}}^{\text{TOTData}}(E_i) - B_{\text{Interacting}}^{\text{Data}}(E_i) = C_{\text{Interacting}}^{\pi MC}(E_i) N_{\text{Interacting}}^{\text{TOTData}}(E_i). \quad (1.3)$$

499 1.4 Estimate of Energy Loss before the TPC

500 The beamline particles travel a path from where their momentum is measured in
 501 the beamline until they are tracked again inside the TPC. In the LArIAT geometry,
 502 a particle leaving the WC4 will encounter the materials listed in Table 1.4 before
 503 being registered again. The energy lost by the particle in this non-instrumented
 504 material modifies the particle's kinetic energy and directly affects the cross section
 505 measurement, as shown in equation 5.

We derive an estimate of the energy loss between the beamline momentum mea-
 surement and the TPC (E_{loss}) from the pion and kaon DDMC samples, since this
 quantity is not measurable directly on data. The E_{loss} distribution for the 60A and

Material	density [g/cm ³]	width [cm]
Fiberglass laminate (G10)	1.7	1.28
Liquid Argon	1.4	3.20
Stainless Steel	7.7	0.23
Titanium	4.5	0.04
Air	$1.2 \cdot 10^{-3}$	89.43
Plastic Scintillator	1.03	1.20 (+ 1.30)

Table 1.4: LArIAT material budget from WC4 to the TPC Front Face.

100A pion sample is shown in figure 1.10, left and right respectively. A clear double peaked structure is visible, which is due to the particles either missing or hitting the HALO paddle: a schematic rendering of this occurrence is shown in figure 1.11. The kinematic at WC4 determines the trajectory of a particle and whether or not it will hit the halo paddle. In figure 1.12, we plot the true horizontal component of the momentum P_x versus the true X position at WC4 for pions missing the halo paddle (left) and for pions hitting the halo paddle (right) for the 60A MC simulation runs – analogous plots are obtained with the 100A simulation. These distributions can be separated drawing a line in this position-momentum space. We use a logistic regression [8] as a classifier to find the best separating line, shown in both plots as the red line. We classify as “hitting the halo paddle” all pions whose P_x and X are such that

$$P_x + 0.02 * X - 0.4 < 0$$

and as “missing the halo paddle” all pions whose P_x and X are such that

$$P_x + 0.02 * X - 0.4 > 0,$$

506 where the coefficients of the line are empirically found by the logistic regression es-
507 timation. Overall, this simple method classifies in the right category (hit or miss)
508 about 86% of the pion events. In MC, we assign $E_{loss} = 32 \pm 4$ MeV for pion events
509 classified as “hitting the halo paddle”; we assign $E_{loss} = 24 \pm 3$ MeV for pion events

classified as “missing the halo paddle”. We apply the same classifier on data. A scan of the simulated geometry showed an excess of 3 cm of uninstrumented argon compared with the surveyed detector geometry. We account for this difference by assigning in data $E_{loss} = 24 \pm 6$ MeV for pion events classified as “hitting the halo paddle” and $E_{loss} = 17 \pm 6$ MeV for pion events classified as “missing the halo paddle”, where the uncertainty is derived as the standard deviation of the double peaked distribution.

The summary of the values for used for E_{Loss} for the pion sample is listed in table 1.5 with the analogous results for the study on the kaon case.

1.5 Tracking Studies

In this section, we describe three studies. The first is a justification of the selection criteria for the beamline handshake with the TPC information. We perform this study to boost the correct identification of the particles in the TPC associated with the beamline information, while maintaining sufficient statistics for the cross section measurement. The second study is an optimization of the tracking algorithm, with the scope of maximizing the identification of the hadronic interaction point inside the TPC. These two studies are related, since the optimization of the tracking is performed on TPC tracks which have been matched to the wire chamber track; in turn, the tracking algorithm for TPC tracks determines the number of reconstructed tracks in each event used to try the matching with the wire chamber track. Starting with

	E_{loss} [MeV]	
	Hitting Halo	Missing Halo
Pion MC	32 ± 4	24 ± 3
Pion Data	25 ± 6	17 ± 6
Kaon MC	37 ± 5	31 ± 4
Kaon Data	26 ± 6	22 ± 6

Table 1.5: Energy loss for pions and kaons.

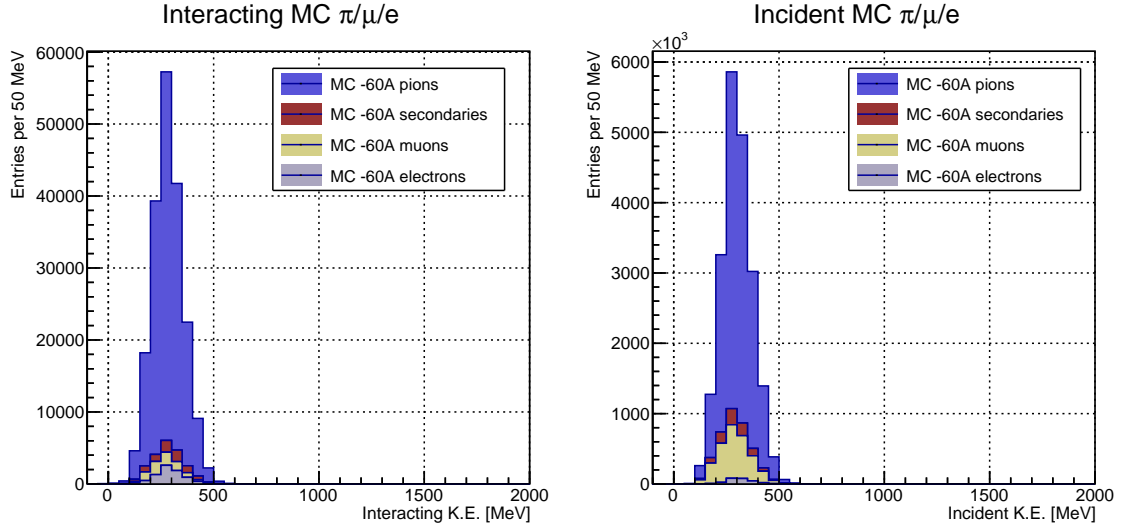


Figure 1.9: Left: staggered contributions to the interacting kinetic energy distribution for electron (grey), muons (yellow) and pion (blue) in the 60A simulation sample. Right: staggered contributions to the incident kinetic energy distribution for electron (grey), muons (yellow) and pion (blue) in the 60A simulation sample.

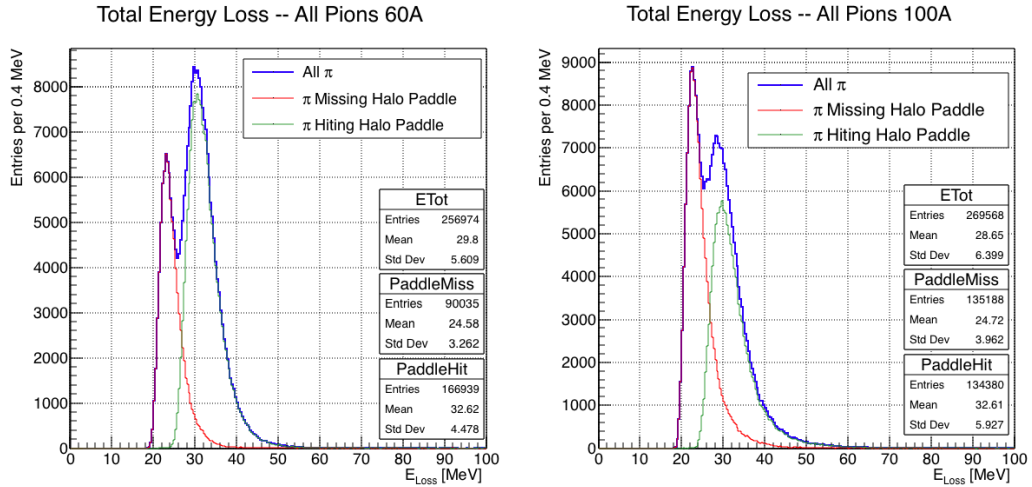


Figure 1.10: True energy loss between WC4 and the TPC front face according to the MC simulation of negative pions of the 60A runs (left) and of the 100A runs (right). The distribution for the whole data sample is shown in blue, the distribution for the pions missing the halo is shown in red, and the distribution for the pions hitting the halo is shown in green.

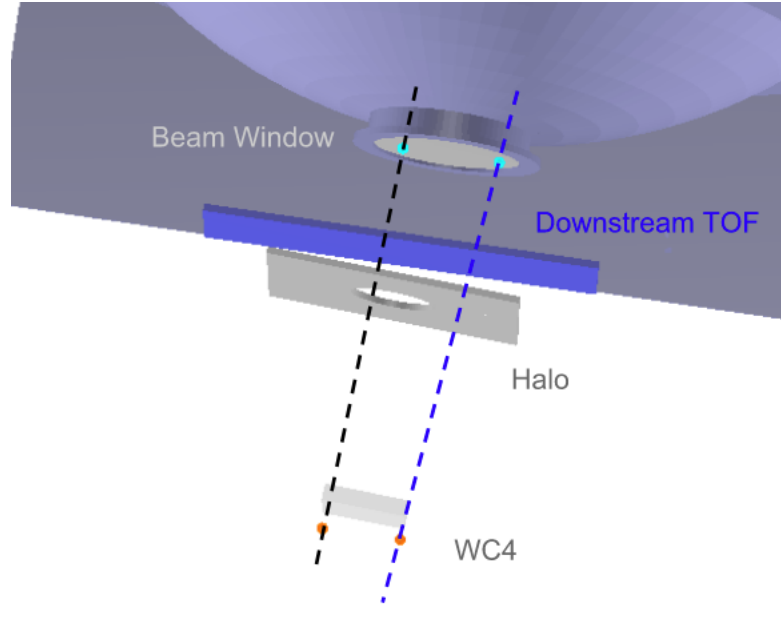


Figure 1.11: Schematic rendering of the particle path between WC4 and the TPC front face. The paddle with the hollow central circle represents the Halo paddle. We illustrate two possible trajectories: in black, a trajectory that miss the paddle and goes through the hole in the Halo, in blue a trajectory that hits the Halo paddle and goes through the scintillation material.

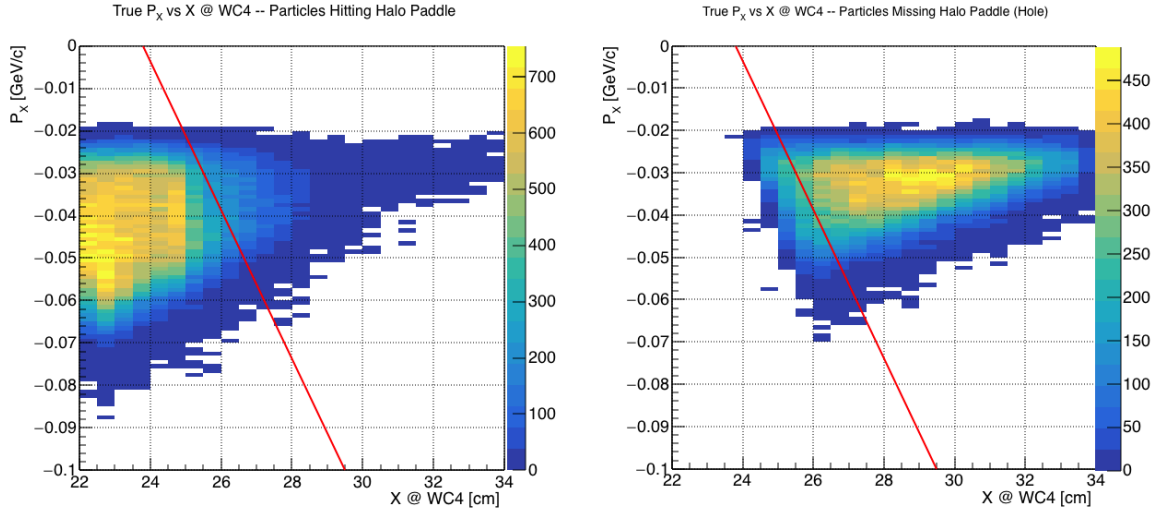


Figure 1.12: Horizontal component of the true momentum vs the horizontal position at WC4 for MC simulated pions of the 60A runs. The plot on the left shows the distribution for pion that miss the halo paddle and the plot on the right shows the distributions for pions that hit the halo. The form of the classifier is overlaid to both plots (red line).

530 a sensible tracking reconstruction, we perform the WC2TPC matching optimization
 531 first, then the tracking optimization. The WC2TPC match purity and efficiency are
 532 then calculated again with the optimized tracking.

533 The third study is an evaluation of the angular resolution of the tracking algorithm
 534 in data and MC, which is particularly important in the context of the cross section
 535 analyses.

536 1.5.1 Study of WC to TPC Match

537 Plots I want in this section:

- 538 1. WC2TPC MC DeltaX, DeltaY and α

539 Scope of this study is assessing the goodness of the wire chamber to TPC match
 540 on Monte Carlo and decide the selection values we will use on data. A word of caution
 541 is necessary here. With this study, we want to minimize pathologies associated with
 542 the presence of the primary hadron itself, e.g. the incorrect association between the
 543 beamline hadron and its decay products inside the TPC. Assessing the contamination
 544 from pile-up², albeit related, is beyond the scope of this study.

545 In MC, we are able to define a correct WC2TPC match using the Geant4 truth
 546 information. We are thus able to count how many times the WC tracks is associated
 547 with the wrong TPC reconstructed track.

548 We define a correct match if the all following conditions are met:

- 549 - the length of the true primary Geant4 track in the TPC is greater than 2 cm,
- 550 - the length of the reconstructed track length is greater than 2 cm,
- 551 - the Z position of the first reconstructed point is within 2 cm from the TPC
 552 front face

2. We remind the reader that the DDMC is a single particle Monte Carlo, where the beam pile up is not simulated.

553 - the distance between the reconstructed track and the true entering point is the
 554 minimum compared with all the other reconstructed tracks.

555 In order to count the wrong matches, we consider all the reconstructed tracks
 556 whose Z position of the first reconstructed point lies within 2 cm from the TPC front
 557 face. Events with true length in TPC < 2 cm are included. Since hadrons are shot
 558 100 cm upstream from the TPC front face, the following two scenarios are possible
 559 from a truth standpoint:

560 [Ta] the primary hadron decays or interact strongly before getting to the TPC,
 561 [Tb] the primary hadron enters the TPC.

562 As described in Section 0.2, we define a WC2TPC match according to the relative
 563 position of the WC and TPC track parametrized with ΔR and the angle between
 564 them, parametrized with α . Once we choose the selection values r_T and α_T to de-
 565 termine a reconstructed WC2TPC match, the following five scenarios are possible in
 566 the truth to reconstruction interplay :

- 567 1) only the correct track is matched
- 568 2) only one wrong track is matched
- 569 3) the correct track and one (or more) wrong tracks are matched
- 570 4) multiple wrong tracks matched.
- 571 5) no reconstructed tracks are matched

572 Since we keep only events with one and only one match, we discard cases 3), 4)
 573 and 5) from the events used in the cross section measurement. For each set of r_T and
 574 α_T selection value, we define purity and efficiency of the selection as follows:

$$\text{Efficiency} = \frac{\text{Number of events correctly matched}}{\text{Number of events with primary in TPC}}, \quad (1.4)$$

$$\text{Purity} = \frac{\text{Number of events correctly matched}}{\text{Total number of matched events}}. \quad (1.5)$$

Figure 1.13 shows the efficiency (left) and purity (right) for WC2TPC match as a function of the radius, r_T , and angle, α_T , selection value. It is apparent how both efficiency and purity are fairly flat as a function of the radius selection value at a given angle. This is not surprising. Since we are studying a single particle gun Monte Carlo sample, the wrong matches can occur only for mis-tracking of the primary or for association with decay products; decay products will tend to be produced at large angles compared to the primary, but could be fairly close to the in x and y projection of the primary. The radius cut would play a key role in removing pile up events.

For LArIAT cross section measurements, we generally prefer purity over efficiency, since a sample of particles of a pure species will lead to a better measurement. Obviously, purity should be balanced with a sensible efficiency to avoid rejecting the whole sample.

We choose $(\alpha_T, r_T) = (8 \text{ deg}, 4 \text{ cm})$ and get a MC 85% efficiency and 98% purity for the kaon sample and a MC 95% efficiency and 90% purity for the pion sample.

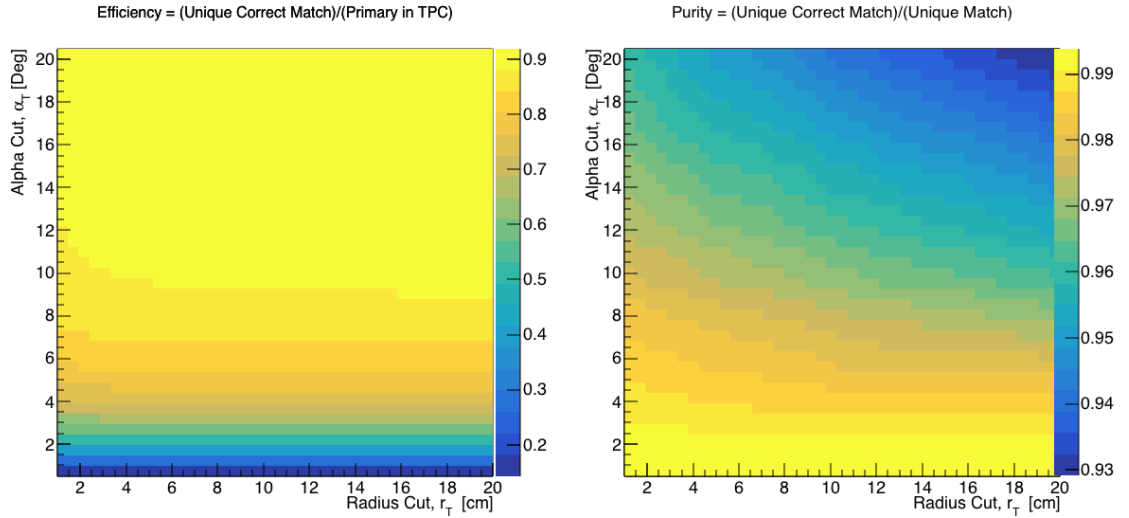


Figure 1.13: Efficiency (left) and purity (right) for WC2TPC match as a function of the radius and angle selections for the kaon sample.

589 1.5.2 Tracking Optimization

590 1.5.3 Angular Resolution

591 Scope of this study is to understand and compare the tracking performances and
592 angular resolution of the TPC tracking on data and MC. We use the angular resolution
593 of the tracking to determine the value of smallest angle that we can reconstruct with
594 a non-zero efficiency, effectively determining a selection on the angular distribution
595 of the cross section measurement due to the tracking performance. This study is
596 performed on the pion sample, but its results are extrapolated to the kaon case.

597 We start by selecting all the WC2TPC matched tracks used for the cross section
598 analysis. These tracks can contain from a minimum of 3 3D-space points to a maxi-
599 mum of 240 3D-space points. We fit a line to all the 3D-space points associated with
600 the track. For each track we calculate the average distance between each point in
601 space and the fit line as follows

$$\bar{d} = \frac{\sum_i^N d_i}{N}, \quad (1.6)$$

602 where N is the number of 3D-space points of the track and d_i is the distance of the
603 i -th space point to the line fit. Several tests to compare the goodness of fit between
604 data and MC have been considered. We decided to use \bar{d} for its straightforward
605 interpretation. The \bar{d} distribution for data and MC is shown in Figure 1.14 and
606 shows a relatively good agreement between data and MC.

607 A visual representation of the procedure used to evaluate the angular resolution is
608 shown in Figure 1.16. For each track, we order the space points according to their Z
609 position along the positive beam direction (panel a) and we split them in two sets: the
610 first set contains all the points belonging to the first half of the track and the second
611 set contains all the points belonging the second half of the track. We remove the last
612 four points in the first set and the first four points in the second set, so to have a
613 gap in the middle of the original track (panel b). We fit the first and the second set

614 of points with two lines (panel c). We then calculate the angle between the fit of the
 615 first and second half α (panel d). The angle α determines the spatial resolution of
 616 the tracking. The distributions for data and MC for α are given in Figure 1.15. The
 617 mean of the data and MC angular resolution are respectively

$$\bar{\alpha}_{Data} = (5.0 \pm 4.5) \text{ deg}, \quad (1.7)$$

$$\bar{\alpha}_{MC} = (4.5 \pm 3.9) \text{ deg}. \quad (1.8)$$

618 Interaction angles smaller than the angle resolution are indistinguishable for the
 619 reconstruction. Therefore, we assess our ability to measure the cross section to be
 620 limited to interaction angles greater than 5.0 deg. More accurate studies of the angular
 621 resolution as a function of the kinetic energy and track length, albeit interesting, are
 622 left for an improvement of the analysis.

623 It is beneficial to take a moment to describe the definition of interaction angle.
 624 In case of elastic scattering, the definition is straightforward: the interaction angle is
 625 the angle between the incoming and outgoing pion, i.e.

$$\theta = \cos^{-1} \left(\frac{\vec{p}_{\text{incoming}} \cdot \vec{p}_{\text{outgoing}}}{|\vec{p}_{\text{incoming}}| |\vec{p}_{\text{outgoing}}|} \right). \quad (1.9)$$

626 In case of inelastic scattering, the presence of several topologies requires a more
 627 complex definition, as shown in figure 1.17. We define the scattering angle as the
 628 biggest of the angles between the incoming pion and the visible daughters, where the
 629 visible daughters are charged particles that travel more than 0.47 cm in the detector
 630 (see panel a); in case all the daughters are invisible, the angle is assigned to be 90
 631 deg (see panel b). We chose this working definition of scattering angle for inelastic
 632 scattering keeping in mind how our tracking reconstruction works: the tracking will
 633 stop correctly in case of all the daughters are not visible in the detector and it is

likely to stop correctly if multiple daughters form an interaction vertex. The only “dangerous” case is the production of one charged daughter plus neutrals, which we can study with this working definition of scattering angle (see panel c).

We can see the effects of the angular resolution on the cross section by plotting the true Geant4 cross section for interaction angles greater than a minimum interaction angle. Figure 1.18 shows the true Geant4 cross section for interaction angles greater than 0 deg (green), 4.5 deg (red), 5.0 deg (blue) and 9.0 deg (yellow). A small 0.5 deg systematic shift between the mean of the data and MC angular resolution is present.

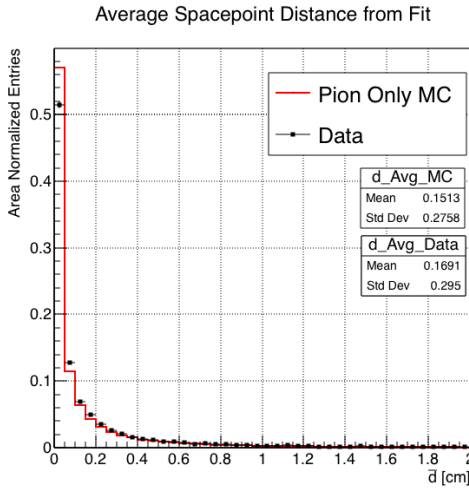


Figure 1.14: Distributions of the average distance between each 3D point in space and the fit line, \bar{d} for the data used in the pion cross section analysis and the pion only DDMC. The distributions are area normalized.

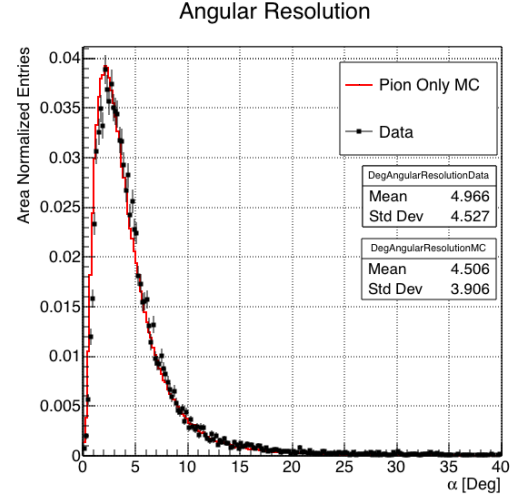


Figure 1.15: Distributions of angular resolution α for data used in the pion cross section analysis and pion only DDMC. The distributions are area normalized.

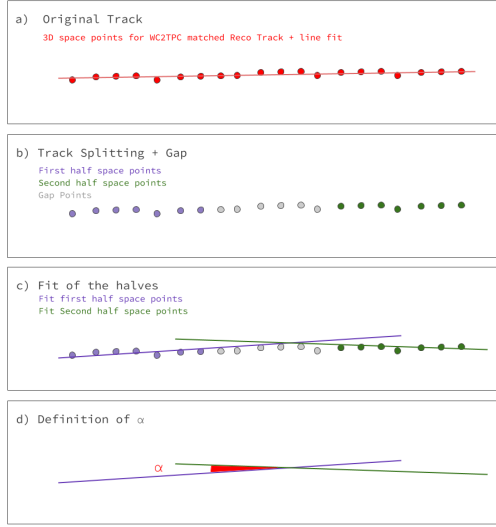


Figure 1.16: A visual representation of the procedure used to evaluate the angular resolution.

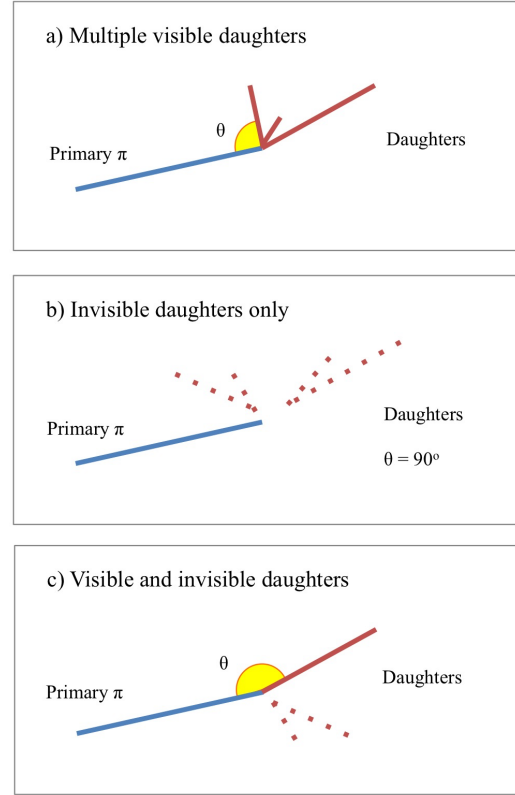


Figure 1.17: A visual representation of the scattering angle definition in case of inelastic scattering.

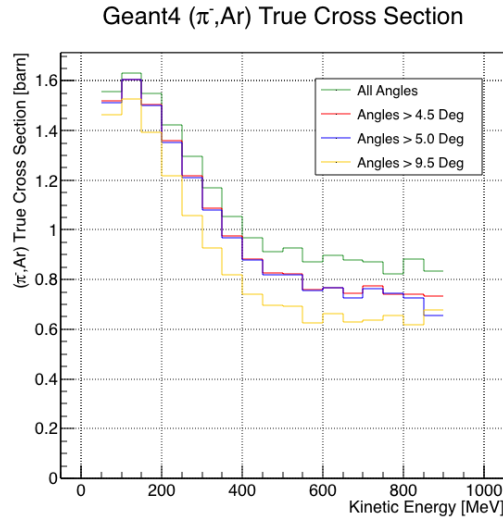


Figure 1.18: True (π^- , Ar) cross section for interaction angles greater than 0 deg (green), 4.5 deg (red), 5.0 deg (blue) and 9.0 deg (yellow).

1.6 Calorimetry Studies

The ability to measure the kinetic energy of hadrons in the TPC is fundamental for the cross section analyses. Thus, we describe first how we calibrate the TPC calorimetric response (Section 1.6.1) and how we measure the kinetic energy of the hadrons in the TPC (Section 1.6.2).

1.6.1 Energy Calibration

Scope of the energy calibration is to identify the factors which convert the charge collected (dQ) to energy deposited in the chamber (dE). As described in section ??, this is a multi-step procedure. In LArIAT, we first correct the raw charge by the electronic noise on the considered wire [44], then by the electron lifetime [45], and then by the recombination using the ArgoNeut recombination values. Lastly, we apply overall calibration of the energy, i.e. we determine the “calorimetry constants” using the procedure described in this section.

We independently determine the calorimetry constants for Data and Monte Carlo in the LArIAT Run-II Data samples using a parametrization of the stopping power (a.k.a. energy deposited per unit length, dE/dX) as a function of momentum. This is done by comparing the stopping power measured on reconstructed quantities against the Bethe-Bloch theoretical prediction for various particle species (see Equation ??). We obtain the theoretical expectation for the dE/dX most probable value of pions (π), muons (μ), kaons (K), and protons (p) in the momentum range most relevant for LArIAT (Figure 1.19) using the tables provided by the Particle Data Group [43] for liquid argon [1].

The basic idea of this calibration technique is to utilize a sample of beamline events with known particle species and momentum to measure the dE/dX of the corresponding tracks in the TPC. In particular, we decided to use positive pions as

667 calibration sample and samples from all the other particle species as cross check. Once
 668 the dE/dX of the positive pion sample has been measured at various momenta, we
 669 tune to calorimetry constants within the reconstruction software to align the measured
 670 values to match the theoretical ones found in Figure 1.19.

671 In data, we start by selecting a sample of beamline positive pion beamline can-
 672 didates without any restriction on their measured momentum³. We then apply the
 673 WC2TPC match and subtract the energy loss upstream to the TPC front face, de-
 674 termining the momentum at the TPC front face. For each surviving pion candidate,
 675 we measure the dE/dx at each of the first 12 spacepoints associated the 3D recon-
 676 structed track, corresponding to a ~ 5 cm portion. These dE/dX measurements are
 677 then put into a histogram that corresponds to measured momentum of the track.
 678 The dE/dX histograms are sampled every 50 MeV/c in momentum (e.g. 150 MeV/c
 679 $< P < 200$ MeV/c, 200 MeV/c $< P < 250$ MeV, etc...). This process of selecting,
 680 sampling, and recording the dE/dX for various momentum bins is repeated over the
 681 entire sample of events, allowing us to collect sufficient statistic in most of the mo-
 682 mentum bins between 150 MeV/c and 1100 MeV/c. On average, pions and muons
 683 only lose ~ 10 MeV in this 5 cm section of the track and protons lose ~ 20 MeV. Thus
 684 choosing 50 MeV/c size bins for our histograms covers the energy spread within those
 685 bins due to energy loss from ionization for all the particle species identifiable in the
 686 beamline. Each 50 MeV/c momentum binned dE/dX histogram is now fit with a
 687 simple Landau function. The most probable value (MPV) and the associated error
 688 on the MPV from the fit are extracted and plotted against the theoretical prediction
 689 Figure 1.19. Depending on the outcome of the data-prediction comparison, we modify
 690 the calorimetry constants and we repeat the procedure until a qualitative agreement
 691 is achieved. We perform this tuning for the collection and induction plane separately.
 692 As a cross check to the calorimetry constants determined using the positive pions,

3. it should be noted that some muon and position contamination is present in the π^+ sample

we lock the constants and plot the dE/dx versus momentum distribution of all the other particle species identifiable in the beamline data ($\pi/\mu/e$, K , p, in both polarities) against the corresponding Beth-Bloch prediction. The agreement between data from the other particle species and the predictions is the expected result of this cross check. The results of the tuning and cross check for Run-II data on the collection plane is shown in Figure 1.20 negative polarity data on top, positive polarity data on the bottom.

In MC, we simulate the corresponding positive pion sample with the DDMC (see section 1.2.2) and follow the same steps as in data. More details on the calorimetry tuning can be found in [33].

Add agreement between data and MC for dedx for pions

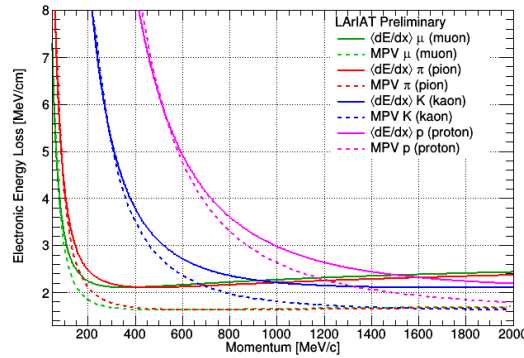


Figure 1.19: Stopping power for pions, muons, kaons, and protons in liquid argon over the momentum range most relevant for LArIAT according to the Beth-Bloch equation. The solid lines represent the prediction for the mean energy dE/dX , while the dashed lines are the predictions for the MPV.

1.6.2 Kinetic Energy Measurement

The measured kinetic energy of a hadron candidate at each argon slab determines which bins of the interacting and incident histograms a selected event is going to fill. In this section, we define the measurement on the kinetic energy and determine the related uncertainty. We will propagate this uncertainty into the cross section

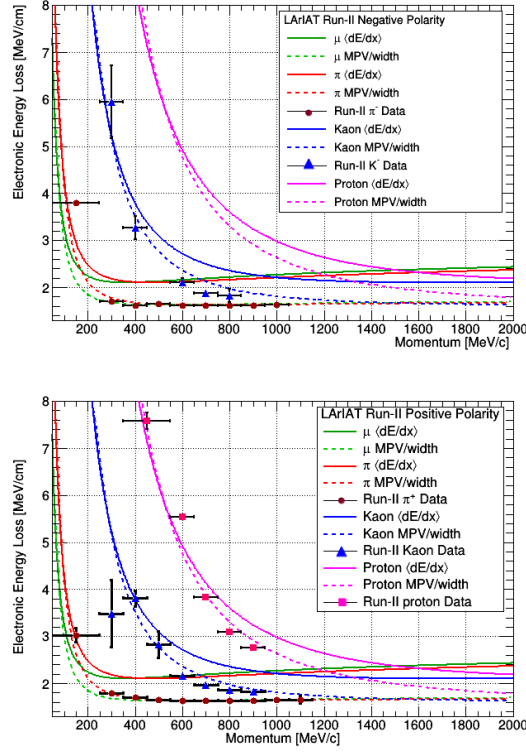


Figure 1.20: Stopping power versus Momentum for Run-II negative (top) and positive (bottom) polarity data. We achieve the agreement between the Bethe-Bloch predictions and the distribution obtained with of the positive pions (top plot, red dots) by tuning the calorimetry constants. Once the calorimetry constants are locked in, the agreement between the other particle species and the Bethe-Bloch predictions follows naturally.

709 measurement, as discussed in Section 2.1.2 for the pion cross section and in Section
 710 ?? for the kaon cross section.

711 The kinetic energy of a hadron at the j^{th} slice of argon in the TPC is given by

$$KE_j = \sqrt{p_{Beam}^2 + m_{Beam}^2} - m_{Beam} - E_{Loss} - E_{FF-j}, \quad (1.10)$$

712 where p_{Beam} is the momentum measured by the beamline detectors, m_{Beam} is the
 713 mass of the hadron as reported in the PDG, E_{Loss} is the energy loss between the
 714 beamline and the TPC, and E_{FF-j} is the energy that the hadron deposited from the

715 TPC front face until the j^{th} slice. The uncertainty on KE_j is then given by

$$\delta KE_j = \sqrt{\delta p_{Beam}^2 + \delta E_{Loss}^2 + \delta E_{\text{dep FF-j}}^2}, \quad (1.11)$$

716 where we have dropped the uncertainty on the mass, since it is orders of magnitude
 717 smaller than the other uncertainties. We assume the relative uncertainty on p_{Beam} to
 718 be 2%, and the uncertainty on the energy loss upstream to be 7 MeV, as calculated
 719 in Section 1.4. We describe the estimate of the uncertainty on $E_{\text{FF-j}}$ in the rest of
 720 this section.

721 The energy deposited by the hadron from the TPC front face until the j^{th} slice is
 722 the sum of the measured energy deposited in each previous slabs E_i , i.e.

$$E_{\text{FF-j}} = \sum_{i < j} E_i, \quad (1.12)$$

723 where E_i is measured in each slab as the product of the stopping power, dE/dX_i ,
 724 and the track pitch, $Pitch_i$, for that point. If we assume conservatively that the
 725 measurements of E_i are not independent from one another, the uncertainty on $E_{\text{FF-j}}$
 726 becomes

$$\delta E_{\text{FF-j}} = (j - 1)\delta E_i, \quad (1.13)$$

727 where δE_i is the uncertainty on the energy loss in one slab of argon.

728 The left side of Figure 1.21 shows the distribution of the energy deposited in each
 729 slab of argon, for the 60A negative pion dataset in black and for the pion only MC
 730 in blue. The analogous plot for the -100A negative pion data set is show on the right
 731 side of Figure 1.21. The distributions are fitted with a landau displayed in red for
 732 data and in teal for MC. The uncertainty on E_i is given by the width of the Landau
 733 fit to the data. A small systematic uncertainty is given by a 1.0% difference between
 734 the most probable value of the landau fits in data and MC.

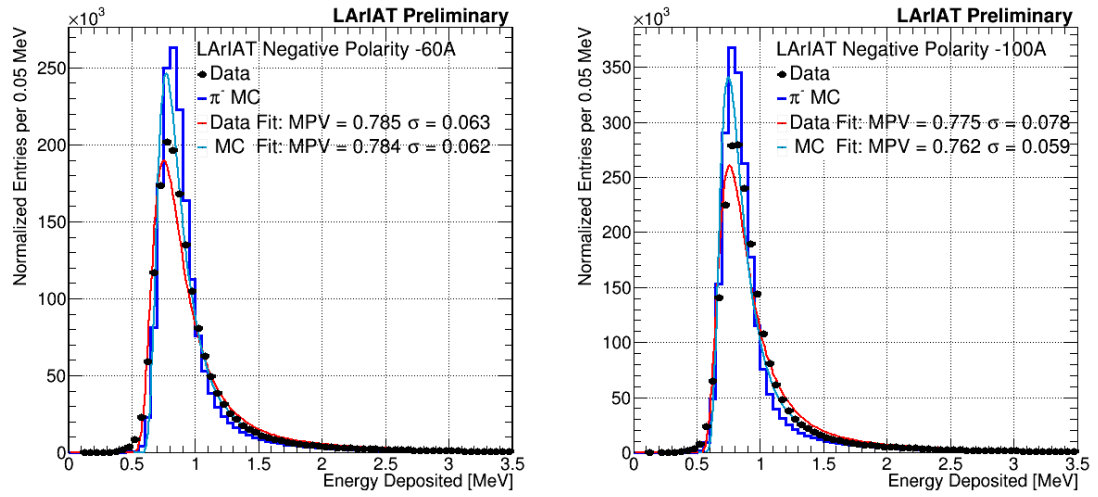


Figure 1.21: Energy deposited E_i in a single slab of argon for the pion -60A runs (left) and -100A runs (right). The data is shown in black, the MC in blue. The distributions are fitted with a landau displayed in red for data and in teal for MC.

Chapter 2

Negative Pion Cross Section Measurement

In this chapter, we show the result of the thin slice method to measure the (π^- -Ar) total hadronic cross section. In Section 2.1, we start by measuring the raw cross section, i.e. the cross section obtained exclusively using data reconstruction, without any additional corrections. In Section 2.2, we apply a statistical subtraction of the background contributions based on simulation and a correction for detection inefficiency. The final results are presented in Section 2.3.

2.1 Raw Cross Section

We measure the raw (π^- -Ar) total hadronic cross section as a function of the kinetic energy in the two chosen data sets, the -60A and -100A negative runs. As we will clarify in Section 2.2, the corrections to the raw cross section depend on the beam conditions and need to be calculated independently for the two datasets. Thus, we present here the measurement of the raw cross section on the two datasets separately.

750 As stated in section 0.3.2, the raw cross section is given by the equation

$$\sigma_{TOT}(E_i) = \frac{1}{n\delta X} \frac{N_{Int}^{TOT}(E_i)}{N_{Inc}^{TOT}(E_i)}, \quad (2.1)$$

751 where N_{Int}^{TOT} is the measured number of particles interacting at kinetic energy E_i ,
 752 N_{Inc}^{TOT} is the measured number of particles incident on an argon slice at kinetic energy
 753 E_i , n is the density of the target centers and δX is the thickness of the argon slice.
 754 The density of the target centers and the slab thickness are $n = 0.021 \cdot 10^{24} \text{ cm}^{-3}$ and
 755 $\delta X = 0.47 \text{ cm}$, respectively.

756 Figure 2.1 shows the distribution of N_{Int}^{TOT} as a function of the kinetic energy for the
 757 60A dataset on the left and for the 100A dataset on the right. The data central points
 758 are represented by black dots, the statistical uncertainty is shown in black, while the
 759 systematic uncertainty is shown in red. Data is displayed over the N_{Int}^{TOT} distribution
 760 obtained with a MC mixed sample of pions, muon and electrons (additional details
 761 on the composition will be provided in Section 2.2.1). The contribution from the
 762 simulated pions is shown in blue, the one from secondaries in red, the one from
 763 muons in yellow and the ones from electrons in gray. The simulated pion's and
 764 backgrounds' contributions are stacked; the sum of the integrals from each particle
 765 species is normalized to the integral of the data.

766 Figure 2.2 shows the distribution of N_{Inc}^{TOT} for the 60A dataset on the left and for
 767 the 100A dataset on the right. Data is displayed over the MC. The same color scheme
 768 and normalization procedure is used for both the interacting and incident histograms.

769 Figure 2.3 shows the raw cross section for the 60A dataset on the left and for the
 770 100A dataset on the right, statistical uncertainty in black and systematic uncertainty
 771 in red. The raw data cross section is overlaid to the reconstructed cross section for
 772 the MC mixed sample, displayed in azure. Since the background contributions and
 773 the detector effects for the 60A and 100A sample are different, it is premature to

774 compare the raw cross sections obtained from the two samples at this point.

775 We describe the calculation of the statistical uncertainty for the interacting, in-
 776 cident and cross section distributions in Section 2.1.1; we describe the procedure to
 777 calculate the corresponding systematics uncertainty on Section 2.1.2.

778 2.1.1 Statistical Uncertainty

779 The statistical uncertainty for a given kinetic energy bin of the cross section is cal-
 780 culated by error propagation from the statistical uncertainty on $N_{\text{Inc}}^{\text{TOT}}$ and $N_{\text{Int}}^{\text{TOT}}$
 781 correspondent bin. Since the number of incident particles in each energy bin is given
 782 by a simple counting, we assume that $N_{\text{Inc}}^{\text{TOT}}$ is distributed as a poissonian with mean
 783 and variance equal to $N_{\text{Inc}}^{\text{TOT}}$ in each bin. On the other hand, $N_{\text{Int}}^{\text{TOT}}$ follows a bino-
 784 mial distribution: a particle in a given energy bin might or might not interact. The
 785 variance for the binomial is given by

$$\text{Var}[N_{\text{Int}}^{\text{TOT}}] = \mathcal{N} P_{\text{Interacting}} (1 - P_{\text{Interacting}}). \quad (2.2)$$

786 Since the interaction probability $P_{\text{Interacting}}$ is $\frac{N_{\text{Int}}^{\text{TOT}}}{N_{\text{Inc}}^{\text{TOT}}}$ and the number of tries \mathcal{N} is
 787 $N_{\text{Inc}}^{\text{TOT}}$, equation 2.2 translates into

$$\text{Var}[N_{\text{Int}}^{\text{TOT}}] = N_{\text{Inc}}^{\text{TOT}} \frac{N_{\text{Int}}^{\text{TOT}}}{N_{\text{Inc}}^{\text{TOT}}} (1 - \frac{N_{\text{Int}}^{\text{TOT}}}{N_{\text{Inc}}^{\text{TOT}}}) = N_{\text{Int}}^{\text{TOT}} (1 - \frac{N_{\text{Int}}^{\text{TOT}}}{N_{\text{Inc}}^{\text{TOT}}}). \quad (2.3)$$

788 $N_{\text{Inc}}^{\text{TOT}}$ and $N_{\text{Int}}^{\text{TOT}}$ are not independent. The statistical uncertainty on the cross
 789 section is thus calculated as

$$\delta\sigma_{TOT}(E) = \sigma_{TOT}(E) \left(\frac{\delta N_{\text{Int}}^{\text{TOT}}}{N_{\text{Int}}^{\text{TOT}}} + \frac{\delta N_{\text{Inc}}^{\text{TOT}}}{N_{\text{Inc}}^{\text{TOT}}} \right) \quad (2.4)$$

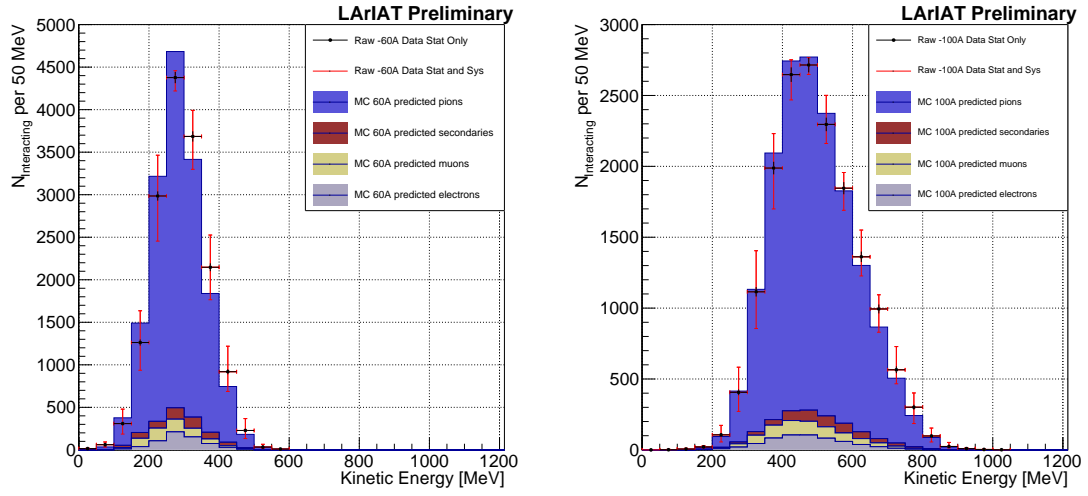


Figure 2.1: Raw number of interacting pion candidates as a function of the reconstructed kinetic energy for the 60A runs (left) and for the 100A runs (right). The statistical uncertainties are shown in black, the systematic uncertainties in red.

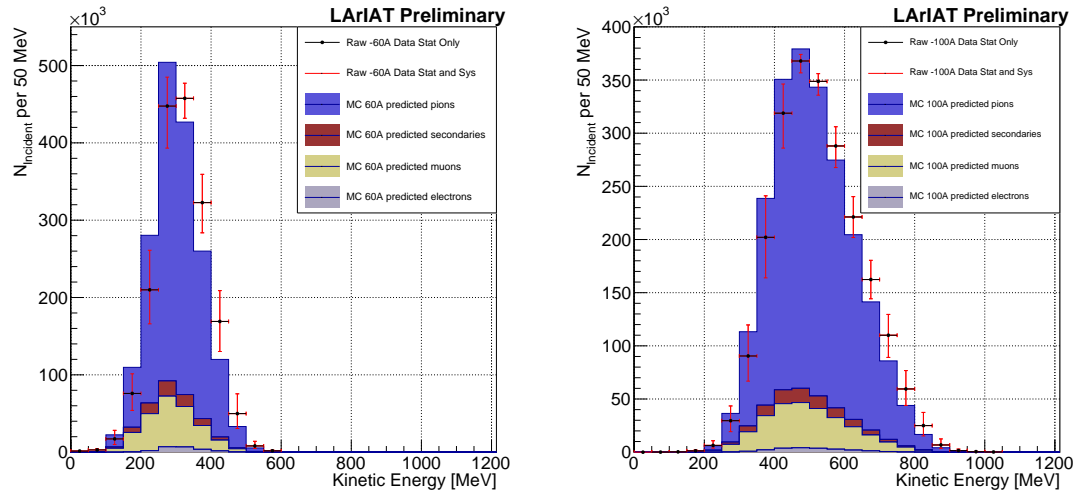


Figure 2.2: Raw number of incident pion candidates as a function of the reconstructed kinetic energy for the 60A runs (left) and for the 100A runs (right). The statistical uncertainty is shown in black, the systematic uncertainties in red.

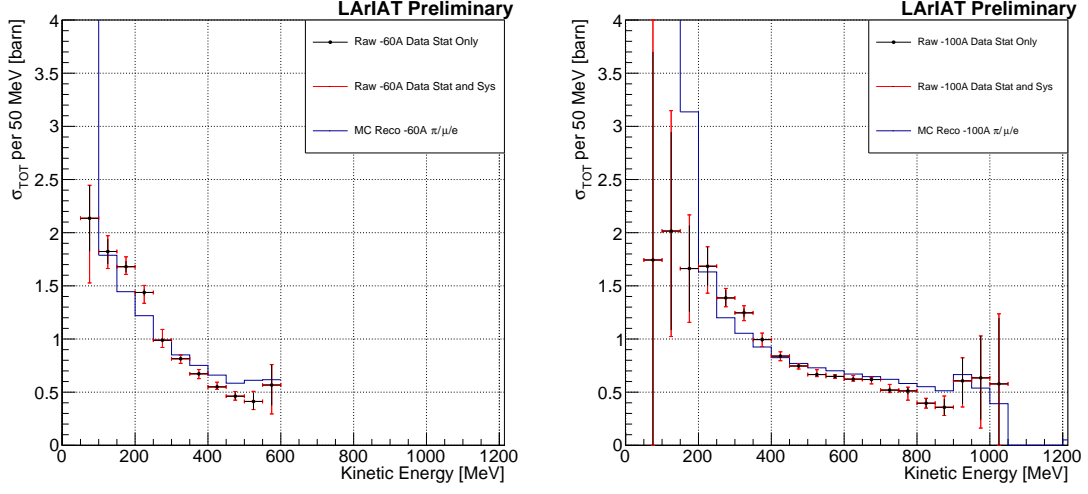


Figure 2.3: Raw (π^- -Ar) total hadronic cross section for the 60A runs (left) and for the 100A runs (right). The statistical uncertainty is shown in black, the systematic uncertainties in red. The raw cross section obtained with a MC mixed sample of pions, muon and electrons in the percentage predicted by G4Beamline is shown in azure.

790 where:

$$\delta N_{\text{Inc}}^{\text{TOT}} = \sqrt{N_{\text{Inc}}^{\text{TOT}}} \quad (2.5)$$

$$\delta N_{\text{Int}}^{\text{TOT}} = \sqrt{N_{\text{Int}}^{\text{TOT}} \left(1 - \frac{N_{\text{Int}}^{\text{TOT}}}{N_{\text{Inc}}^{\text{TOT}}} \right)}. \quad (2.6)$$

791 2.1.2 Treatment of Systematics

792 The only systematic effect considered in the measurement of the raw cross section
 793 results from the propagation of the uncertainty associate with the measurement of
 794 the kinetic energy at each argon slab. As shown in Section 1.6.2, the uncertainty on
 795 the kinetic energy of a pion candidate at the j^{th} slab of argon is given by

$$\delta KE_j = \sqrt{\delta p_{\text{Beam}}^2 + \delta E_{\text{Loss}}^2 + \delta E_{\text{dep FF-j}}^2} \quad (2.7)$$

$$= \sqrt{(2\% p_{\text{Beam}})^2 + (\sim 6 \text{ [MeV]})^2 + (j-1)^2 (\sim 0.08 \text{ [MeV]})^2}. \quad (2.8)$$

796 We propagate this uncertainty by varying the energy measurement KE_j at each
797 argon slab. We measure $N_{\text{Inc}}^{\text{TOT}}$, $N_{\text{Int}}^{\text{TOT}}$ and the cross section in three cases: first
798 assigning the measured KE_j at each kinetic energy sampling, then assigning $KE_j +$
799 δKE_j , and finally assigning $KE_j - \delta KE_j$. The difference between the values obtained
800 using the KE_j sampling and the maximum and minimum values in each kinetic energy
801 bin determines the systematic uncertainty.

802 2.2 Corrections to the Raw Cross Section

803 As described in section 0.3.3 a series of corrections are needed to derive the true
804 pion cross section from the raw cross section. The corrected cross section is given in
805 equation 9,

$$\sigma_{TOT}^{\pi^-}(E_i) = \frac{1}{n\delta X} \frac{\epsilon^{\text{Inc}}(E_i)}{\epsilon^{\text{Int}}(E_i)} \frac{C_{\text{Int}}^{\pi MC}(E_i)}{C_{\text{Inc}}^{\pi MC}(E_i)} \frac{N_{\text{Int}}^{\text{TOT}}(E_i)}{N_{\text{Inc}}^{\text{TOT}}(E_i)}. \quad (9)$$

806 Section describes the procedure employed to obtain $C_{\text{Int}}^{\pi MC}(E_i)$ and $C_{\text{Inc}}^{\pi MC}(E_i)$ and
807 the propagation to the cross section measurement of the relative uncertainties.

808 Section describes the procedure employed to obtain $\epsilon^{\text{Int}}(E_i)$ and $\epsilon^{\text{Inc}}(E_i)$ and the
809 propagation to the cross section measurement of the relative uncertainties.

810 2.2.1 Background subtraction

811 Even if pions are by far the biggest component of the beam in negative polarity
812 runs, the LArIAT beam is not a pure pion beam. While useful to discriminate pi-
813 ons/muons/electrons from kaons, and protons, the beamline detectors are not sensi-
814 tive enough to discriminate among the lighter particles in the beam: electrons, muons
815 and pions fall under the same mass hypothesis. Thus, we need to assess the back-
816 ground from beamline particles other than pions in the event selections used for the
817 pion cross section analysis and correct for its effects.

818 **Beam Composition**

819 We define beamline background every TPC track matched to the WC track which is
820 not a primary pion. Potentially, there are 4 different types of beamline background:

- 821 1) electrons,
- 822 2) muons,
- 823 3) secondaries from pion events,
- 824 4) matched pile up events.

825 The first step is to estimate what percentage of events used in the cross section
826 calculation is not a primary pion. The next two sections will illustrate this estimate
827 for the electrons, muons and secondaries from pion event. We estimate the last type
828 of background, the “matched pile up” events, to be a negligible fraction, because of
829 the definition of the WC2TPC match: we deem the probability of a single match with
830 a halo particle in the absence of a beamline particle¹ negligibly small. **SHOW VTX**
831 **distribution in WC2TPC match**

832 **Background from Beamline Electrons and Muons**

833 We estimate the percentage of electrons and muons in the beam via the G4Beamline
834 MC. Since the beamline composition is a function of the magnet settings, we simulate
835 separately events for magnet current of -60A and -100A. Table 2.1 shows the beam
836 composition per magnet setting after the mass selection according to the G4Beamline
837 simulation.

1. Events with multiple WC2TPC matches are always rejected.

Figure 2.4: Beam composition for the -60A runs (left) and -100A runs (right). The solid blue plot represents the simulated pion content, the yellow plot represents the simulated muon content and the grey plot represents the simulated electron content. The plots are area normalized to the number of data events, shown in red.

Figure 2.4 shows the momentum predictions from G4Beamline overlaid with data for the 60A runs (left) and for the 100A runs (right). The predictions for electrons, muons and pions have been staggered and their sum is area normalized to data, which is shown in red. Albeit not perfect, these plots show a reasonable agreement between the momentum shapes in data and MC. We attribute the difference in shape to the lack of simulation of the WC efficiency in the MC which is momentum dependent and leads to enhance the number events in the center of the momentum distribution.

Once the beam composition at WC4 is know, we simulate the electrons, muons and pions with the DDMC and we subject the three samples to the same selection chain (WC2TPC match, shower filter, pile up filter). The percentage of electrons and muons surviving the selection chain weighted by the beam composition is the electron and muon background in the pion cross section sample, as shown in Table 1.3.

Background from secondaries at TPC Front Face

Pions can travel the length of the LArIAT beamline and interact hadronically in the steel or in the non-instrumented argon upstream to the TPC front face. Or, they could decay in flight between WC4 and the TPC. One of the interaction products can leak into the TPC and be matched with the WC track, contributing to the pool of events used for the cross section calculation. We call this type of particles “secondaries” from pion events, with a terminology inspired by Geant4. We estimate the number of secondaries using the DDMC pion sample. The percentage of secondaries is given by the number of matched WC2TPC tracks whose corresponding particle is not flagged as primary by Geant4. The secondary to pion ratio is 4.9% in the 60A sample and $Y\%$ in the 100A sample.

2.2.2 Background Contribution to the Cross Section

Figures 2.5 show $C_{Interacting}^{\pi MC}(E_i)$ and $C_{Incident}^{\pi MC}(E_i)$ as a function of the kinetic energy for the 60A runs and their systematic uncertainty. We take a 100% systematic uncertainty on the muon and electron content: we calculate the extreme values of $C_{Interacting}^{\pi MC}(E_i)$ and $C_{Incident}^{\pi MC}(E_i)$ in each bin changing the beam composition for the configurations listed in Table 2.2.

Treatment of Systematics

2.2.3 Efficiency Correction

The interaction point for a track used in the total hadronic cross section analysis is defined to be the last point of the WC2TPC matched track which lies inside the fiducial volume. This definition is independent from the topology of the interaction. If the TPC track stops within the fiducial volume, its last point will be the interaction point, no matter what the products of the interaction look like; if the track crosses the boundaries of the fiducial volume, the track will be considered “through going” and no interaction point will be found. Given this definition, it is evident that we rely on the tracking algorithm to discern where the interaction occurred in the TPC and correctly stop the tracking. The tracking algorithm has an intrinsic angle resolution as shown in section 1.5.3, which limits its efficiency, especially in the case of elastic scattering occurring at low angles. Thus, we need to apply an efficiency correction to data in order to retrieve the true cross section. The efficiency correction is evaluated separately for the interacting and incident histograms, namely ϵ_i^{int} and ϵ_i^{inc} , and propagated to the cross section as shown in equation 8.

883 Efficiency Correction: Procedure

884 We describe here the procedure to calculate the efficiency correction taking the in-
 885 teracting histogram as example and noting that the procedure is identical for the
 886 incident histogram.

887 We derive the correction on a set of pure pion MC, calculating its value bin by
 888 bin as the ratio between the true bin content and the correspondent reconstructed
 889 bin content. The correction is then applied to the relevant bin in data. In formulae,
 890 the efficiency correction is calculated to be

$$\epsilon_i^{\text{int}} = \frac{N_{\text{Interacting}}^{\pi \text{ Reco MC}}(E_i)}{N_{\text{Interacting}}^{\pi \text{ True MC}}(E_i)}, \quad (2.9)$$

891 where $N_{\text{Interacting}}^{\pi \text{ True MC}}(E_i)$ is the content of the i -th bin in for the true interacting
 892 histogram, and $N_{\text{Interacting}}^{\pi \text{ Reco MC}}(E_i)$ is the content of the i -th bin in for the reconstructed
 893 interacting histogram. The correction is applied to data as follows

$$N_{\text{Interacting}}^{\pi \text{ True Data}}(E_i) = \frac{N_{\text{Interacting}}^{\pi \text{ Reco Data}}(E_i)}{\epsilon_i^{\text{int}}} = N_{\text{Interacting}}^{\pi \text{ Reco Data}}(E_i) \frac{N_{\text{Interacting}}^{\pi \text{ True MC}}(E_i)}{N_{\text{Interacting}}^{\pi \text{ Reco MC}}(E_i)}. \quad (2.10)$$

894 where $N_{\text{Interacting}}^{\pi \text{ Reco Data}}(E_i)$ is the background subtracted bin content of the i -th bin in
 895 for the reconstructed interacting histogram for data, i.e.

$$N_{\text{Interacting}}^{\pi \text{ Reco Data}}(E_i) = N_{\text{Interacting}}^{\text{TOT Data}}(E_i) - B_{\text{Interacting}}^{\text{Data}}(E_i) = C_{\text{Interacting}}^{\pi \text{ MC}}(E_i) N_{\text{Interacting}}^{\text{TOT Data}}(E_i). \quad (2.11)$$

896 Figures ?? show $\epsilon_i^{\text{int}}(E_i)$ and $\epsilon_i^{\text{int}}(E_i)$ as a function of the kinetic energy for the
 897 60A runs and their systematic uncertainty.

898 In section 1.5.3, we estimated the angular resolution for data and MC to be
 899 $\bar{\alpha}_{\text{Data}} = (5.0 \pm 4.5)$ deg and $\bar{\alpha}_{\text{MC}} = (4.5 \pm 3.9)$ deg, respectively. Interaction angles
 900 smaller than the angular resolution are indistinguishable for the reconstruction. Thus,

901 we claim we are able to measure the cross section for interaction angles greater than
902 5.0 deg. Geant4 simulates interactions at all angles, as shown in figure ?? . In order
903 to calculate the efficiency correction, we select events which have an interaction angle
904 greater than a given α_{res} to construct the true interacting and incident histograms
905 (the denominator of the efficiency correction).

906 The systematics on the efficiency correction is estimated by varying the value of
907 α_{res} to be

908 **Treatment of Systematics**

	I = -60 A	I = -100 A
G4Pions	68.8 %	87.4 %
G4Muons	4.6 %	3.7 %
G4Electrons	26.6 %	8.9 %

Table 2.1: Simulated beamline composition per magnet settings

	Magnet Current -60A			Magnet Current -100 A		
	MC π^-	MC μ^-	MC e^-	MC π^-	MC μ^-	MC e^-
Composition 2x muons	64.2 %	9.2 %	26.6 %	83.7 %	7.4 %	8.9 %
Composition 0.5x muons	71.1 %	2.3 %	26.6 %	89.2 %	1.9 %	8.9 %
Composition 2x Electrons	42.2 %	4.6 %	53.2 %	78.5 %	3.7 %	17.8 %
Composition 0.5x Electrons	82.1 %	4.6 %	13.3 %	91.9 %	3.7 %	4.4 %

Table 2.2: Beam composition variation for the study of systematics due to beam contamination.

Figure 2.5: Left: relative pion content for interacting histogram a function of kinetic energy for the 60A runs, statistics uncertainty in azure and systematic uncertainty in blue. Right: relative pion content for incident histogram a function of kinetic energy for the 60A runs, statistics uncertainty in azure and systematic uncertainty in blue.

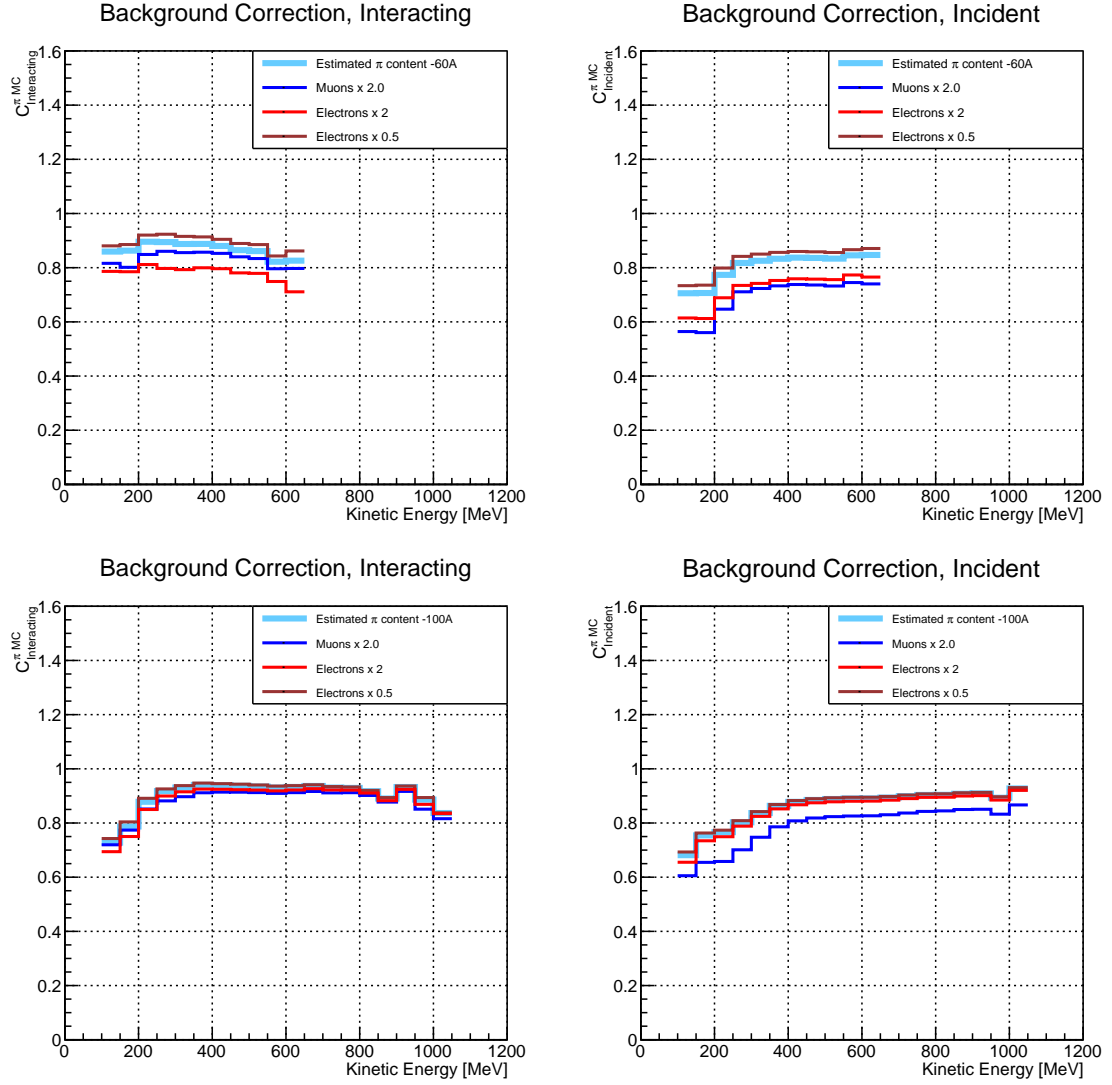


Figure 2.6: .

909 2.3 Results

910 Figure 2.7 show the measurement of the (π^- -Ar) total hadronic cross section for
911 scattering angles greater than 5° , as the result of the background subtraction and
912 efficiency correction to the raw cross section. The top left plot is the measurement
913 obtained on the 60A data, statistical uncertainty in black and systematic uncertainty
914 in red. The top right plot is the measurement obtained on the 100A data, statistical
915 uncertainty in black and systematic uncertainty in blue. The bottom plot shows the
916 two measurements overlaid. In all three plot, the Geant4 prediction for the total
917 hadronic cross section for angle scattering greater than 5° is displayed in green.

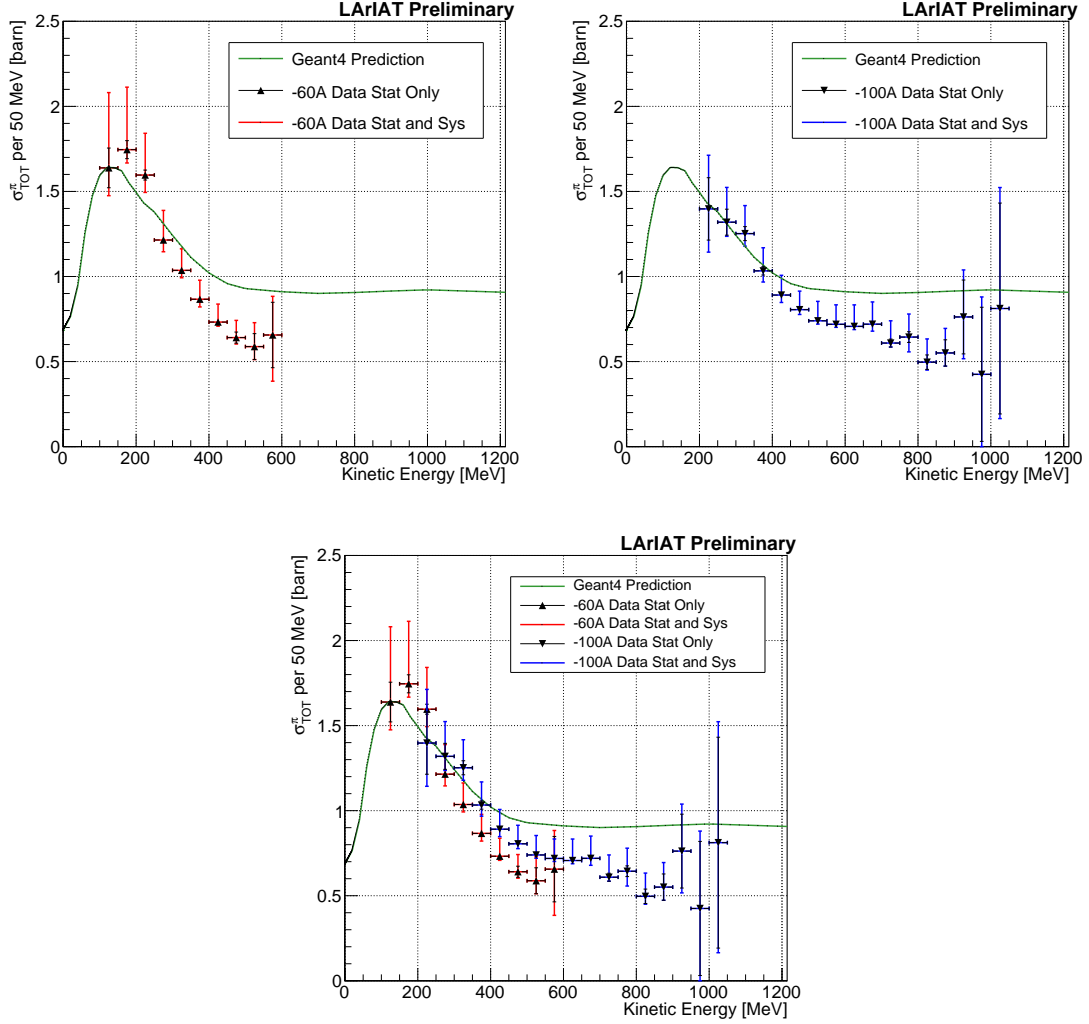


Figure 2.7: *Top Left:* (π^- -Ar) total hadronic cross section for scattering angles greater than 5° measured in the 60A sample, statistical uncertainty in black and systematic uncertainty in red. The Geant4 prediction for the total hadronic cross section for angle scattering greater than 5° is displayed in green.

Top Right: (π^- -Ar) total hadronic cross section for scattering angles greater than 5° measured in the 100A sample, statistical uncertainty in black and systematic uncertainty in blue. The Geant4 prediction for the total hadronic cross section for angle scattering greater than 5° is displayed in green.

Bottom: (π^- -Ar) total hadronic cross section measurements in the 60A and 100A samples overlaid with the Geant4 prediction (green).

Bibliography

[1] PDG Tables for Liquid Argon. . Technical report.

[2] R Acciarri, C Adams, J Asaadi, B Baller, T Bolton, C Bromberg, F Cavanna, E Church, D Edmunds, A Ereditato, S Farooq, B Fleming, H Greenlee, G Horton-Smith, C James, E Klein, K Lang, P Laurens, D McKee, R Mehdiyev, B Page, O Palamara, K Partyka, G Rameika, B Rebel, M Soderberg, J Spitz, A M Szelc, M Weber, M Wojcik, T Yang, and G P Zeller. A study of electron recombination using highly ionizing particles in the argoneut liquid argon tpc. *Journal of Instrumentation*, 8(08):P08005, 2013.

[3] R Acciarri, M Antonello, B Baibussinov, M Baldo-Ceolin, P Benetti, F Calaprice, E Calligarich, M Cambiaghi, N Canci, F Carbonara, F Cavanna, S Centro, A G Cocco, F Di Pompeo, G Fiorillo, C Galbiati, V Gallo, L Grandi, G Meng, I Modena, C Montanari, O Palamara, L Pandola, G B Piano Mortari, F Pietropaolo, G L Raselli, M Roncadelli, M Rossella, C Rubbia, E Segreto, A M Szelc, S Ventura, and C Vignoli. Effects of nitrogen contamination in liquid argon. *Journal of Instrumentation*, 5(06):P06003, 2010.

[4] R. Acciarri et al. Design and Construction of the MicroBooNE Detector. *JINST*, 12(02):P02017, 2017.

[5] R. Acciarri et al. First Observation of Low Energy Electron Neutrinos in a Liquid Argon Time Projection Chamber. *Phys. Rev.*, D95(7):072005, 2017. [Phys.

938 Rev.D95,072005(2017)].

939 [6] M Adamowski, B Carls, E Dvorak, A Hahn, W Jaskierny, C Johnson, H Jostlein,
 940 C Kendziora, S Lockwitz, B Pahlka, R Plunkett, S Pordes, B Rebel, R Schmitt,
 941 M Stancari, T Tope, E Voirin, and T Yang. The liquid argon purity demonstrator.
 942 *Journal of Instrumentation*, 9(07):P07005, 2014.

943 [7] C. Adams et al. The Long-Baseline Neutrino Experiment: Exploring Fundamen-
 944 tal Symmetries of the Universe. 2013.

945 [8] Alan Agresti. *Categorical Data Analysis*. Wiley Series in Probability and Statis-
 946 tics. Wiley, 2013.

947 [9] A. Aguilar-Arevalo et al. Evidence for neutrino oscillations from the observa-
 948 tion of anti-neutrino(electron) appearance in a anti-neutrino(muon) beam. *Phys.*
 949 *Rev.*, D64:112007, 2001.

950 [10] A. A. Aguilar-Arevalo et al. Improved Search for $\bar{\nu}_\mu \rightarrow \bar{\nu}_e$ Oscillations in the
 951 MiniBooNE Experiment. *Phys. Rev. Lett.*, 110:161801, 2013.

952 [11] S. Amoruso et al. Study of electron recombination in liquid argon with the
 953 ICARUS TPC. *Nucl. Instrum. Meth.*, A523:275–286, 2004.

954 [12] C. Anderson et al. The ArgoNeuT Detector in the NuMI Low-Energy beam line
 955 at Fermilab. *JINST*, 7:P10019, 2012.

956 [13] M. Antonello, B. Baibussinov, P. Benetti, E. Calligarich, N. Canci, S. Cen-
 957 tro, A. Cesana, K. Cieslik, D. B. Cline, A. G. Cocco, A. Dabrowska, D. De-
 958 qual, A. Dermenev, R. Dolfini, C. Farnese, A. Fava, A. Ferrari, G. Fiorillo,
 959 D. Gibin, S. Gninenko, A. Guglielmi, M. Haranczyk, J. Holeczek, A. Ivashkin,
 960 J. Kisiel, I. Kochanek, J. Lagoda, S. Mania, A. Menegolli, G. Meng, C. Monta-
 961 nari, S. Otwinowski, A. Piazzoli, P. Picchi, F. Pietropaolo, P. Plonski, A. Rap-

962 poldi, G. L. Raselli, M. Rossella, C. Rubbia, P. Sala, A. Scaramelli, E. Seg-
 963 reto, F. Sergiampietri, D. Stefan, J. Stepaniak, R. Sulej, M. Szarska, M. Ter-
 964 rani, F. Varanini, S. Ventura, C. Vignoli, H. Wang, X. Yang, A. Zalewska, and
 965 K. Zaremba. Precise 3d track reconstruction algorithm for the ICARUS t600 liq-
 966 uid argon time projection chamber detector. *Advances in High Energy Physics*,
 967 2013:1–16, 2013.

968 [14] M. Antonello et al. A Proposal for a Three Detector Short-Baseline Neutrino
 969 Oscillation Program in the Fermilab Booster Neutrino Beam. 2015.

970 [15] C. Athanassopoulos et al. Evidence for $\nu(\mu) \rightarrow \nu(e)$ neutrino oscillations
 971 from LSND. *Phys. Rev. Lett.*, 81:1774–1777, 1998.

972 [16] B. Baller. Trajcluster user guide. Technical report, apr 2016.

973 [17] Gary Barker. Neutrino event reconstruction in a liquid argon TPC. *Journal of*
 974 *Physics: Conference Series*, 308:012015, jul 2011.

975 [18] J B Birks. Scintillations from organic crystals: Specific fluorescence and relative
 976 response to different radiations. *Proceedings of the Physical Society. Section A*,
 977 64(10):874, 1951.

978 [19] Mark G. Boulay and A. Hime. Direct WIMP detection using scintillation time
 979 discrimination in liquid argon. 2004.

980 [20] W. M. Burton and B. A. Powell. Fluorescence of tetraphenyl-butadiene in the
 981 vacuum ultraviolet. *Applied Optics*, 12(1):87, jan 1973.

982 [21] E. Church. LArSoft: A Software Package for Liquid Argon Time Projection Drift
 983 Chambers. 2013.

984 [22] The LArIAT Collaboration. The liquid argon in a testbeam (lariat) experiment.
 985 Technical report, In Preparation 2018.

- [23] S.E. Derenzo, A.R. Kirschbaum, P.H. Eberhard, R.R. Ross, and F.T. Solmitz. Test of a liquid argon chamber with 20 m rms resolution. *Nuclear Instruments and Methods*, 122:319 – 327, 1974.
- [24] A Ereditato, C C Hsu, S Janos, I Kreslo, M Messina, C Rudolf von Rohr, B Rossi, T Strauss, M S Weber, and M Zeller. Design and operation of argontube: a 5 m long drift liquid argon tpc. *Journal of Instrumentation*, 8(07):P07002, 2013.
- [25] R. Acciarri et al. Convolutional neural networks applied to neutrino events in a liquid argon time projection chamber. *Journal of Instrumentation*, 12(03):P03011, 2017.
- [26] R. Acciarri et al. Design and construction of the MicroBooNE detector. *Journal of Instrumentation*, 12(02):P02017–P02017, feb 2017.
- [27] C. E. Aalseth et al.l. DarkSide-20k: A 20 tonne two-phase LAr TPC for direct dark matter detection at LNGS. *The European Physical Journal Plus*, 133(3), mar 2018.
- [28] V.M. Gehman, S.R. Seibert, K. Rielage, A. Hime, Y. Sun, D.-M. Mei, J. Maassen, and D. Moore. Fluorescence efficiency and visible re-emission spectrum of tetraphenyl butadiene films at extreme ultraviolet wavelengths. *Nuclear Instruments and Methods in Physics Research Section A: Accelerators, Spectrometers, Detectors and Associated Equipment*, 654(1):116 – 121, 2011.
- [29] H. Geiger and E. Marsden. On a diffuse reflection of the formula-particles. *Proceedings of the Royal Society A: Mathematical, Physical and Engineering Sciences*, 82(557):495–500, jul 1909.
- [30] C. Green, J. Kowalkowski, M. Paterno, M. Fischler, L. Garren, and Q. Lu. The Art Framework. *J. Phys. Conf. Ser.*, 396:022020, 2012.

- [31] H J Hilke. Time projection chambers. *Reports on Progress in Physics*, 73(11):116201, 2010.
- [32] N. Ishida, M. Chen, T. Doke, K. Hasuike, A. Hitachi, M. Gaudreau, M. Kase, Y. Kawada, J. Kikuchi, T. Komiyama, K. Kuwahara, K. Masuda, H. Okada, Y.H. Qu, M. Suzuki, and T. Takahashi. Attenuation length measurements of scintillation light in liquid rare gases and their mixtures using an improved reflection suppresser. *Nuclear Instruments and Methods in Physics Research Section A: Accelerators, Spectrometers, Detectors and Associated Equipment*, 384(2-3):380–386, jan 1997.
- [33] G. Pulliam J. Asaadi, E. Gramellini. Determination of the electron lifetime in lariat. Technical report, August 2017.
- [34] George Jaffé. Zur theorie der ionisation in kolonnen. *Annalen der Physik*, 347(12):303–344, 1913.
- [35] B J P Jones, C S Chiu, J M Conrad, C M Ignarra, T Katori, and M Toups. A measurement of the absorption of liquid argon scintillation light by dissolved nitrogen at the part-per-million level. *Journal of Instrumentation*, 8(07):P07011, 2013.
- [36] Benjamin J. P. Jones. *Sterile Neutrinos in Cold Climates*. PhD thesis, MIT, 2015.
- [37] M A Leigui de Oliveira. Expression of Interest for a Full-Scale Detector Engineering Test and Test Beam Calibration of a Single-Phase LAr TPC. Technical Report CERN-SPSC-2014-027. SPSC-EOI-011, CERN, Geneva, Oct 2014.
- [38] W. H. Lippincott, K. J. Coakley, D. Gastler, A. Hime, E. Kearns, D. N. McKinsey, J. A. Nikkel, and L. C. Stonehill. Scintillation time dependence and pulse shape discrimination in liquid argon. *Phys. Rev. C*, 78:035801, Sep 2008.

- 1035 [39] M. Mooney. The microboone experiment and the impact of space charge effects.
1036 2015.
- 1037 [40] E. Morikawa, R. Reininger, P. Görtler, V. Saile, and P. Laporte. Argon, krypton,
1038 and xenon excimer luminescence: From the dilute gas to the condensed phase.
1039 *The Journal of Chemical Physics*, 91(3):1469–1477, aug 1989.
- 1040 [41] D. R. Nygren. The time projection chamber: A new 4 π detector for charged
1041 particles. Technical report, 1974.
- 1042 [42] L. Onsager. Initial recombination of ions. *Phys. Rev.*, 54:554–557, Oct 1938.
- 1043 [43] C. Patrignani et al. Review of Particle Physics. *Chin. Phys.*, C40(10):100001,
1044 2016.
- 1045 [44] T. Yang R. Acciarri. Investigation of the non-uniformity observed in the wire
1046 response to charge in lariat run 1. Technical report, February 2017.
- 1047 [45] T. Yang R. Acciarri, M. Stancari. Determination of the electron lifetime in lariat.
1048 Technical report, March 2016.
- 1049 [46] C. Rubbia. The Liquid Argon Time Projection Chamber: A New Concept for
1050 Neutrino Detectors. 1977.
- 1051 [47] R. K. Teague and C. J. Pings. Refractive index and the lorentz-lorenz function
1052 for gaseous and liquid argon, including a study of the coexistence curve near the
1053 critical state. *The Journal of Chemical Physics*, 48(11):4973–4984, jun 1968.
- 1054 [48] J. Thomas and D. A. Imel. Recombination of electron-ion pairs in liquid argon
1055 and liquid xenon. *Phys. Rev. A*, 36:614–616, Jul 1987.
- 1056 [49] N Yahlali, L M P Fernandes, K Gonzlez, A N C Garcia, and A Soriano. Imaging
1057 with sipms in noble-gas detectors. *Journal of Instrumentation*, 8(01):C01003,
1058 2013.